FAKULTA STROJNÍHO INŽENÝRSTVÍ
VYSOKÉ UČENÍ TECHNICKÉ V BRNĚ

Developments in quantitative light microscopy applied to cell biology and cancer research

Vývoj kvantitativní světelné mikroskopie aplikované v buněčné biologii a nádorovém výzkumu

Ing. Daniel Zicha, CSc.

Habilitation thesis

Applied Physics

Habilitační práce

Aplikovaná fyzika

Brno 2024

Abstract

This habilitation thesis overviews the scientific activity of the author, which has been focusing on developments in light microscopy, and its applications in addressing mechanisms of cell biology and cancer progression. The developments stem from theoretical principles, including the theory of moments, diffusion theory, interference theory, statistics of directional data, graph theory, fluorescence correlation spectroscopy, and fluorescence resonance energy transfer. The applications cover measurements of cell invasion, cell motility, cellular morphology, chemotaxis, intracellular transport, molecular size, and interactions. The results include the discovery of a novel metastasis suppressor, protein 4.1B, and the mechanism of its action was also elucidated. Additional results reveal mechanisms of GAB1 protein, kindlin-3 protein, ephrin-B2 protein, mutant connexin 31 proteins in deafness/neuropathy and skin diseases, and WASp protein in Wiskott-Aldrich syndrome. The future directions will mainly focus on developments of Holographic Incoherent-light-source Quantitative Phase Imaging and correlative microscopy with biomedical applications, especially in cancer research with a potential for personalized cancer treatment. The habilitation thesis references a selection of 18 authored and co-authored publications in international scientific journals.

Key Words

Light microscopy, biophysics, cell invasion, cell motility, cellular morphology, chemotaxis, intracellular transport, molecular size and interactions, theory of moments, diffusion theory, interference theory, statistics of directional data, graph theory, fluorescence correlation spectroscopy, fluorescence resonance energy transfer.

Souhrn

Autor této habilitační práce prezentuje přehled své vědecké práce, která je zaměřena na vývoj ve světelné mikroskopii, a její aplikace při zkoumání mechanismů buněčné biologie a nádorové progrese. Vývoj využívá teoretické principy zahrnující teorii momentů, teorii difuze, interferenční teorii, statistiku směrových dat, teorii grafů, fluorescenční korelační spektroskopii a fluorescenční rezonanční transfer energie. Aplikace se zabývají měřením invazivity buněk, buněčné motility, buněčné morfologie, chemotaxe, nitrobuněčného transportu, velikosti molekul a jejich interakcí. Výsledky zahrnují objev nového inhibitoru metastáz, proteinu 4.1B, a mechanismu jeho účinku. Další výsledky odkrývají mechanismy účinku proteinu GAB1, proteinu kindlin-3, proteinu ephrin-B2, proteinů connexin 31 s mutacemi podmiňujícími hluchotu/neuropatii a onemocnění kůže, a proteinu WASp, jehož mutace determinuje Wiskott-Aldrich syndrom. Budoucí výhled bude zaměřen převážně na vývoj holografického kvantitativního zobrazování s nekoherentním zdrojem světla a korelativní mikroskopie pro biomedicínské aplikace zejména ve výzkumu nádorového onemocnění s potenciálem pro personalizovanou léčbu. Tato habilitační práce obsahuje odkazy na 18 vybraných publikací z mezinárodních vědeckých časopisů s autorstvím nebo spoluautorstvím.

Klíčová slova

Světelná mikroskopie, biofyzika, invazivita buněk, buněčná motilita, buněčná morfologie, chemotaxe, nitrobuněčný transport, velikost molekul a jejich interakce, teorie momentů, teorie difuze, interferenční teorie, statistika směrových dat, teorie grafů, fluorescenční korelační spektroskopie a fluorescenční rezonanční transfer energie.

CONTENTS

1. ABOUT THE AUTHOR

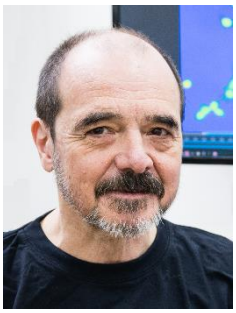

The entire professional career of the author has been spent developing, applying, and teaching advanced light microscopy methods and image processing of particular relevance to cell biology and cancer research. In total, he has published 51 research papers with 4,005 citations. He has a record of interdisciplinary projects. In a partnership with Nikon, he developed a TIRF prototype with automatic adjustment of the evanescence wave thickness using a stepper motor. Nikon subsequently launched a commercial version. He delivered 40 invited lectures at international conferences. He has co-authored four invited reviews and eight book chapters on microscopy techniques and their applications. He has refereed numerous manuscripts for a range of journals, including Science, Journal of Cell Science, Experimental Cell Research, and Journal of Microscopy. Over 17 years of work as head of the Light Microscopy core facility at Imperial Cancer Research Fund, Cancer Research UK London Research Institute, and The Francis Crick Institute, Lincoln's Inn Fields Laboratory has given him extensive experience with leading a team of 7 people, development of microscopy techniques and biological research. He recruited 12 members of staff and established 21 complex imaging systems. Institute grants centrally funded the laboratories. This is why he only had a limited number of grants. Also, core facilities had limited numbers of students and postdoctoral fellows. After his start in the group of Experimental Biophotonics, at the Institute of Mechanical Engineering, CEITEC Brno University of Technology, he was awarded an MSCA grant from the Ministry of Education, Youth and Sports to work on a Strategy for personalized cancer treatment based on live-cell dry-mass profiling. He was teaching at the Faculty of Mechanical Engineering, Brno University of Technology, Czech Republic; The Danish Research School of Molecular Mechanisms of Disease, BRIC, Copenhagen, Denmark; University of York, UK; Department of Biomedical Sciences, University of Copenhagen, Denmark; University of Leeds, UK; Weizmann Institute of Science, Rehovot, Israel; Imperial Cancer Research Fund/ Cancer Research UK London Research Institute/ The Francis Crick Institute, Lincoln's Inn Fields Laboratories; Kingston University, London, UK; Trans-European Tele-Education Network, Europace, Madrid, Spain; and King’s College London UK. He supervised postdoctoral fellows, Ph.D. students, undergraduate students, and A-level students within the Nuffield Research Placement program, where one of the students was awarded the prestigious Gold Crest Award for the project.

2. INTRODUCTION

Principles of physics have always had significant potential in biological research. The author of this thesis spent eight years at the Biophysics department of King's College London, where Rosalind Franklin and Maurice Wilkins used X-ray diffraction to solve the DNA structure, and Jean Hanson pursued early developments in electron microscopy to co-discover the sliding filament theory explaining the muscle contraction. Maurice Wilkins received Nobel Prize for the achievement in 1962. Jean Hanson was elected a Fellow of the Royal Society in 1967. Dramatic developments followed the DNA structure discovery in molecular genetics, and electron microscopy also experienced major advances. A complete understanding of complex biological phenomena requires a parallel effort in functional analysis with live specimens in order to complement the well-defined molecular and structural knowledge.

Light microscopy provides the tools for precisely that. Both Nobel Prize winners, Maurice Wilkins and Andrew Huxley, who co-discovered the sliding filament theory with Jean Hanson, have already worked on light microscopy and interference microscopy (Davies and Wilkins, 1952). Utilizing recent developments in digital cameras, motorization, and software, which opened new possibilities for significant progress in the field, the author contributed especially to quantitative fluorescence and interference microscopy and their applications in biomedical research.

His interest in cancer metastasis has driven the main thread in the research of the author. Cancer metastasis is a dynamic process determined by the motile activity of the cancer cells. Quantitative time-lapse analysis with live cancer cells using light microscopy is a powerful research tool. The author focused on the developments of novel light microscopy techniques, which subsequently proved helpful for other biological problems.

The techniques include the development of novel observation chambers, namely, flow chambers simulating the situation in blood vessels and a chemotaxis chamber (Zicha et al., 1991) mimicking gradients of chemicals in the body. Important developments were in the analysis of the acquired time-lapse sequences. Fluorescence sequences with 3D stacks required novel algorithms allowing quantitation of cell invasion. The results showed mechanical stimulation of invasion by the shear forces in the flow chamber (Hagglund et al., 2009).

Application of the developed techniques allowed the discovery of a novel metastasis suppressor, protein 4.1B, which reduces cell motility and chemotaxis (Cavanna et al., 2007). Therefore, its loss in cancer cells promotes invasion and metastasis.

The techniques facilitated the elucidation of other molecular mechanisms in diseases. Flow experiments with B leukocytes, a type of white blood cells, revealed that their initial attachment to the inner wall of blood vessels, mediated by integrin LFA-1, is entirely dependent on the presence of kindlin-3 protein in the B cells (Willenbrock et al., 2013). Wiskott-Aldrich syndrome was shown to be determined by abrogated chemotaxis (Zicha et al., 1998) in macrophages (Jones et al., 2002).

Special attention was given to developments of phase-shifting interference microscopy for quantitative phase imaging with incoherent-light-source, which features unprecedented accuracy of measurements for the growth of individual cells and their motility (Dunn and Zicha, 1993). The developments included bespoke image analysis and data processing (Zicha and Dunn, 1995), and the application demonstrated significant reductions in growth and motility with human A549 lung

cancer cells with an experimental drug, GDC0941. In contrast, the other three tested drugs did not significantly reduce both parameters (Zicha, 2022). The results open the possibility of utilization of this technique for pre-testing cancer drugs with biopsy-derived cells for personalized cancer treatment. Holographic quantitative phase imaging with an incoherent light source using the Q-Phase microscope (Telight) was used, with further developments of the image processing software, for chronic lymphocytic leukemia cells. The results showed that the GAB1 protein is essential for their motility and contributed to the conclusion that it can be a promising target for treatment (Seda et al., 2021).

High content screening is a valuable complementation to the slower time-lapse analysis and usually relies on end-point evaluation with fixed cells. The author designed and implemented a novel test based on distances between cells in an observation field. When the cells are seeded initially at low density, and the distances are selected on the principle of minimum spanning tree, the sum of the selected distances can be used as an indirect measure of their motility (Zicha and Pardo, 2009). Another application of high content screening was with vascular smooth muscle cells, where automatic analysis of their morphology revealed that the lack of ephrin-B2 protein was responsible for increased cell polarity necessary for increased motility (Foo et al., 2006).

The motile behavior of cells results from intracellular dynamics, and several projects addressed this aspect, leading to the development of Fluorescence Localisation After Photobleaching. This new technique allowed for the first time to reveal the fast intracellular transport of actin molecules essential for the rapid motility of metastatic cells (Zicha et al., 2003). Connexin 31 mutations were shown to affect cell-cell signaling in deafness/neuropathy. The defective signaling was directly measured by quantifying the transport of small fluorescent molecules between cells (Di et al., 2002). Surprisingly, skin defects with connexin mutations were found to be mediated by cell death resulting from stress, and cell-cell transport did not play a role (Tattersall et al., 2009). The binding efficiency between different connexin 31 mutant proteins was characterized (Di et al., 2005) by Fluorescence Resonance Energy Transfer with spectral unmixing, a novel combination of established techniques (Gu et al., 2004). An empirically developed transfection vector was characterized by Fluorescence Correlation Spectroscopy. A newly developed procedure processed the data, and the diameter of the transfection vector particle was determined as 38 nm (Mustapa et al., 2007).

This thesis references a selection of 18 authored and co-authored publications which are grouped in sections according to their topics. The topics are introduced in the relevant sections. The majority of figures in this thesis are adaptations of figures from the related publications.

3. CELL INVASION AND MOTILITY ASSAYS

3.1. Cancer cells

Metastasis is the most severe complication of cancer (Fares et al., 2020). Metastases form by spreading cancer cells from primary tumors to distant parts of the organisms. The process is referred to as the metastatic cascade and involves changes in cell morphology and active cell motility with complex underlying changes in gene expression. As the process involves changes in cell motility implicated in cancer invasion, special procedures based on light microscopy are effective research tools.

3.1.1. Publication I: Addressing cancer invasion and cell motility with quantitative light microscopy

Zicha, D. (2022). *Sci. Rep.* **12**, 1621.

Open access link to full text:
https://www.nature.com/articles/s41598-022-05307-7

Abstract
The incidence of death caused by cancer has been increasing worldwide. The growth of cancer cells is not the main problem. The majority of deaths are due to invasion and metastasis, where cancer cells actively spread from primary tumors. Our inbred rat model of spontaneous metastasis revealed dynamic phenotype changes in vitro correlating with the metastatic potential in vivo and led to a discovery of a metastasis suppressor, protein 4.1B, which affects their 2D motility on flat substrates. Subsequently, others confirmed 4.1B as metastasis suppressor using knock-out mice and patient data suggesting mechanism involving apoptosis. There is evidence that 2D motility may be differentially controlled to the 3D situation. Here we show that 4.1B affects cell motility in an invasion assay similarly to the 2D system, further supporting our original hypothesis that the role of 4.1B as metastasis suppressor is primarily mediated by its effect on motility. This is encouraging for the validity of the 2D analysis, and we propose Quantitative Phase Imaging with incoherent light source for rapid and accurate testing of cancer cell motility and growth to be of interest for personalized cancer treatment as illustrated in experiments measuring responses of human adenocarcinoma cells to selected chemotherapeutic drugs.

Author comments on publication I (Zicha, 2022)

This single-author publication overviews the main research direction of the author. It presents novel 3D measurements of cell invasion as this has a potential of revealing novel aspects (Dalecká et al., 2021; Huang et al., 2020; Meyer et al., 2012), and developments of Incoherent-light-source Quantitative Phase Imaging for anti-cancer drug testing.

The 3D invasion test was based on the author's previous development in a corresponding author paper (Hagglund et al., 2009).

3.1.2. Publication II: Novel shear flow assay provides evidence for non-linear modulation of cancer invasion

Hagglund, S., Hoppe, A., Aubyn, D., Cavanna, T., Jordan, P. and Zicha, D. (2009). *Front Biosci (Landmark Ed)* **14**, 3085–3093.

Open access link to full text:
https://www.imrpress.com/journal/FBL/14/8/10.2741/3437

Abstract

Cancer is a frequent disease in western countries and there is no effective treatment for metastasis, the main cause of death in cancer patients. The situation can be improved by a better understanding of the cancer invasion process. In order to reveal new aspects of this dynamic process, we developed a novel direct viewing cancer cell invasion assay with shear flow in vitro. This assay comprised of a custom-made flow chamber, specially developed cell labelling, high-resolution wide-field microscopy and image-processing-based quantitation. We applied this assay to metastatic rat sarcoma cells which invaded monolayers of rat endothelial cells. Our findings showed that after adhesion, the sarcoma cells initially invaded significantly faster under flow conditions compared to situations without shear stress. Later, however, the rate of invasion under flow decreased and the sarcoma cells without shear stress achieved significantly higher levels of invasion. Our observations thus revealed the non linear modulation of a cancer cell invasion process by shear flow, demonstrating that cancer cells can respond to flow by enhancement of invasiveness similarly to white blood cells.

Author comments on publication II (Hagglund et al., 2009)

This flow test was designed to investigate the crossing of metastatic cancer cells through the blood vessel wall using an *in vitro* model and led to the conclusion that the shear force stimulates early invasion. In contrast, without the flow, the crossing process is slower and most likely eventually dominated by the action of proteolytic enzymes. A bespoke flow chamber insert (Figure 1) was designed and manufactured to be used with a glass-bottom Petri dish (MatTek).

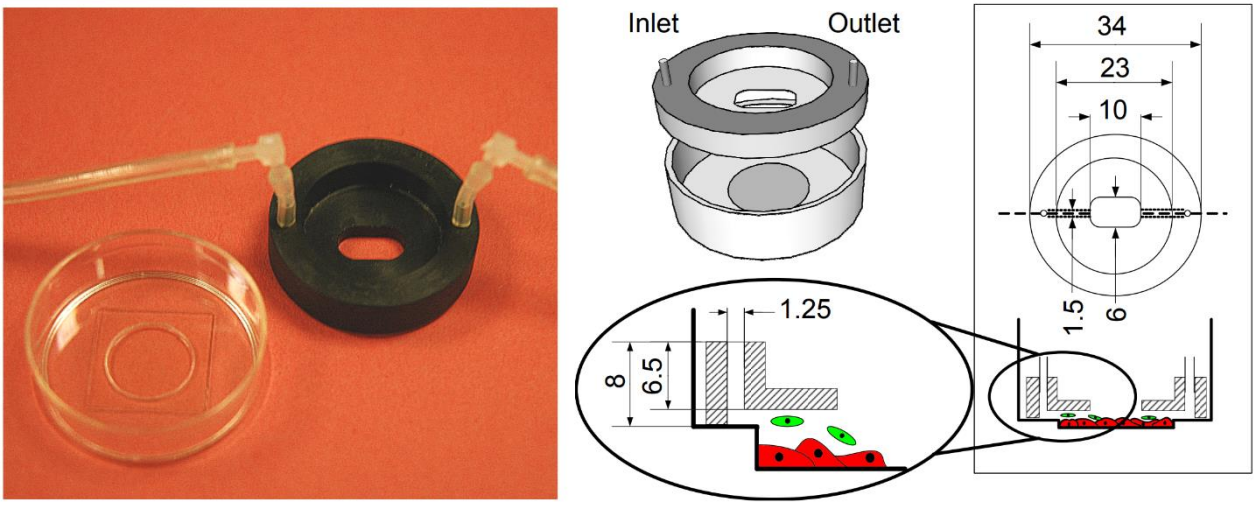

Figure 1. Flow chamber for invasion assay custom produced as an insert for glass bottom MatTek Petri dish. Dimensions are in mm. Floating metastatic cancer cells were labeled with green Vybrant DiO (Invitrogen), and a monolayer of endothelial cells adherent to the glass bottom was labeled with CellTracker Orange CMTMR (Invitrogen).

The tubing was connected to a peristaltic pump, and shear force was calculated according to Equation

$$P = e\,\frac{d}{t.h} \tag{1}$$

where the variables and their values are in Table 1.

Dynamic viscosity for water	e = 0.653 mN s m^{-2}
Travel distance of a particle	d = 50 µm
Observation time	t = 0.277 s
Height above the substrate	h = 8 µm
Shear force	P = 14.7 dynes cm^{-2}

Table 1. Calculation of shear force.

The behavior of the cells was observed by the time-lapse acquisition of z-stacks with a Nikon TE2000 inverted microscope equipped with 63× NA 1.45 objective lens and a CCD camera (Cascade-II, Photometrics), filter wheels (Lambda 10-3, Sutter) and a motorized stage (MS2000, ASI). An intelligent microscopy time-lapse acquisition routine was developed and implemented in Metamorph software. Green fluorescence images were acquired from a manually preselected set of confluent monolayer positions using the motorized stage in multi-field mode. And only when adherent green cells were detected, the acquisition of z-stacks commenced at the specific fields.

While the non-metastatic cells were never seen to cross the monolayer of epithelial cells, the metastatic sarcoma cells were crossing readily (Figure 2).

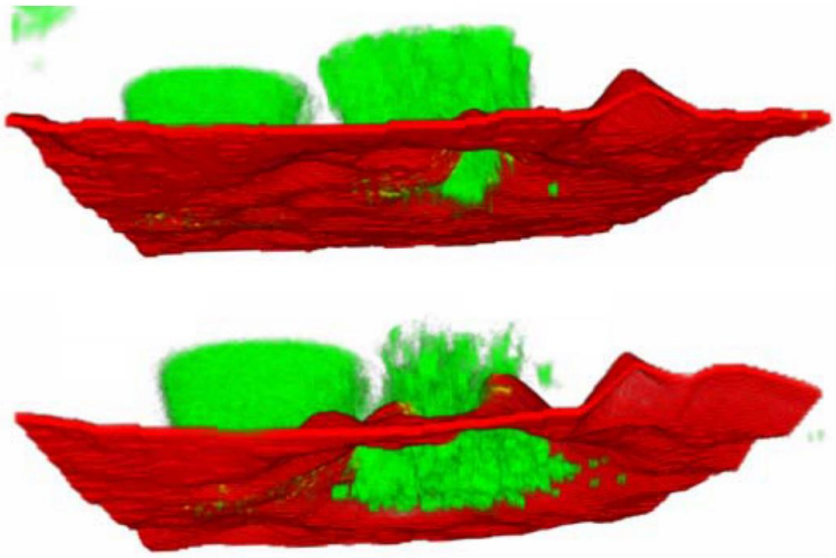

Figure 2. Reconstructed images of an invasion event. The green metastatic sarcoma cell at the right invades under the surface of the monolayer of red-labeled endothelial cells. The left-hand-side adhering green sarcoma cell is not invading. The top part illustrates the early invasion stage, and the bottom part the late invasion stage. The imaging volume was 51 µm x 51 µm x 12 µm.

In order to quantify the invasion process, two parameters were designed and evaluated. The first parameter, “Relative Invasion” (*RI*), reflects the fraction of the volume of an invading cell under the upper surface of the endothelial cells according to Equation

$$RI = \frac{\sum_{<x,y>\in\Omega_I} Max_{z=1}^{U(x,y)} I(x,y,z)}{\sum_{<x,y>\in\Omega_C} Max_{z=1}^{Top} I(x,y,z)} \quad (2)$$

where I is the intensity in the image provided by the scientific CCD camera at voxel (x, y, z), $U(x, y)$ is the automatically detected z-position of the upper surface of the endothelial cells, Ω_C is the projected area of the whole cell, while Ω_I is the projected area of the invaded part the green cell under the surface of the red monolayer.

While the flow situation showed lower *RI* initially, in the end, the control situation without flow achieved significantly higher *RI* of 0.623 ± 0.041, N = 9 compared to 0.443 ± 0.043, N = 13 for flow. Mann-Whitney P-value < 0.014 (Figure 3). Mean ± SEM (Standard Error of the Mean) presented.

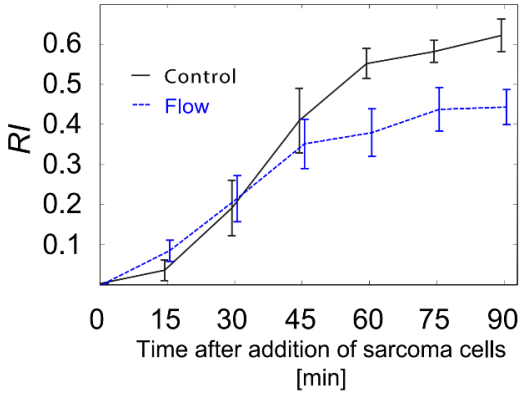

Figure 3. Relative invasion of metastatic cells with and without flow as a function of time.

The second parameter, “Opening Rate of the Endothelial Monolayer” (*OREM*), quantifies the reduction of the fluorescence signal of the endothelial cell in a 4 µm × 4 µm area where the invasion commenced and is defined by Equation

$$OREM = I_{norm}(t_1) - I_{norm}(t_2) \quad (3)$$

where

$$I_{norm}(t) = \frac{I(t) - \mathrm{Min}(I)}{\mathrm{Max}(I) - \mathrm{Min}(I)} \quad (4)$$

and t is time in the time-lapse recording, t_1 was taken as 0 min and t_2 as 30 min, I is intensity in the image, and Min and Max were taken over the 30 min time-lapse period. The signal was measured from the minimum projection of the image z-stacks. *OREM* measurements showed significantly enhanced invasion by flow at 30 min (Figure 4).

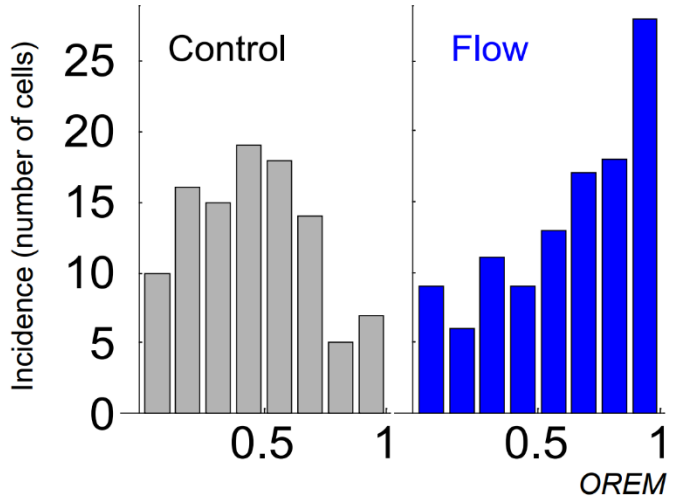

2 × 2 contingency table

OREM value	Low (<0.5)	High (≥0.5)
No flow control	60	44
Flow	35	76

χ^2 P-value < 0.005

Figure 4. Distributions of the incidence of invading cells according to achieved OREM for t_1 = 0 min and t_2 = 30 min and statistical test demonstrating significantly enhanced invasion by flow at 30 min.

Continuation of author comments on publication I (Zicha, 2022)

In the Scientific Reports publication I, the test was applied without the flow to metastatic carcinoma cells, where their expression of the 4.1B protein was manipulated, as illustrated in Figure 5.

3.1.3. Publication III: Evidence for protein 4.1B acting as a metastasis suppressor

Cavanna, T., Pokorná, E., Veselý, P., Gray, C. and Zicha, D. (2007). *J. Cell Sci.* **120**, 606-616.

Open access link to full text:
https://journals.biologists.com/jcs/article/120/4/606/29863

Abstract

We compared a non-metastasising sarcoma cell population with three related populations of increasing metastatic potential. The metastatic cells in vitro exhibited a significantly reduced incidence of actin stress fibres but enhanced motility and chemotaxis. We also investigated gene expression underlying progression to a metastatic phenotype by performing a microarray analysis of the four sarcoma populations. We identified a subset of genes with significantly altered expression levels between non metastasising and metastasising cells in tissue culture and in primary tumours. One such gene, encoding protein 4.1B, is downregulated in the metastatic sarcoma populations. To investigate possible roles of 4.1B in the mechanisms of metastasis, we used RNA interference (RNAi) to reduce its expression in the non-metastatic cells. Cells with reduced 4.1B expression displayed an altered F-actin morphology, with significantly fewer stress fibres. We also found that the 4.1B RNAi cells migrated at twice the speed of the untreated cells. Metastatic cells exogenously expressing 4.1B migrated at half the speed of control metastatic cells and displayed suppressed chemotaxis. Therefore, we propose that the reduction of 4.1B in the metastatic cells promotes the metastatic phenotype as a result of inducing a loss of actin stress fibres and a concomitant increase in cell motility.

Author comments on publication III (Cavanna et al., 2007)

The 4.1B protein was previously discovered as a novel metastasis suppressor in a corresponding author publication (Cavanna et al., 2007) based on protein expression profiling, 2D cell motility and *in vivo* experiments.

Continuation of author comments on publication I (Zicha, 2022)

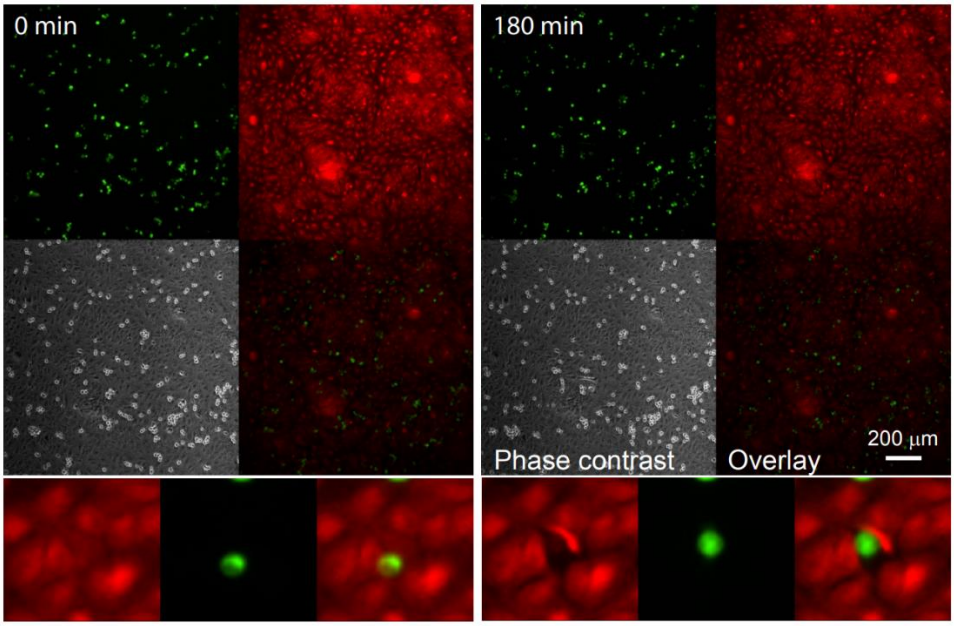

Figure 5. Example images from the time-lapse recording of metastatic carcinoma cells (green) on top of a monolayer of epithelial cells (red) acquired at 15-min lapse interval using 24-well plates on a Nikon TE2000 microscope equipped with 10× NA 0.3 objective lens under Metamorph software control. The full field of view is in the top part, and details of one invasion event are in the bottom part.

This time, only the numbers of invading cells with significant non-zero values of *OREM* were scored as a fraction of all green cells detected. Results are summarized in Table 2.

Treatment	The fraction of invading cells Mean ± SEM	Number of movies	Total number of cells	ANOVA P-value
Control	0.207 ± 0.050	17	1616	reference
4.1B protein	0.031 ± 0.006	17	1361	< 0.5
4.1B inhibition	0.255 ± 0.042	7	622	n.s.

Table 2. The presence of 4.1B protein in the cells significantly enhanced the invasion confirming that the 4.1B metastasis suppressor abrogated 3D motility. The inhibition of the residual 4.1B protein did not significantly enhance the invasion, which is not surprising because the metastatic carcinoma cells did not contain much even before the experiment.

Since the 3D cell motility assay produced consistent results with the previously published measurements of 2D motility, an effort was exerted for more accurate measurements of 2D motility based on Incoherent-light-source Quantitative Phase Imaging.

The technique was based on a previously developed DRIMAPS (Digitally Recorded Interference Microcopy with Automated Phase Shifting) system presented in a co-author publication (Dunn and Zicha, 1993).

3.1.4. Publication IV: Phase-Shifting Interference Microscopy Applied to the Analysis of Cell Behavior

Dunn, G. A. and Zicha, D. (1993). *Cell Behav. Adhes. Motil.* **47**, 91–106.

Open access link:
https://pubmed.ncbi.nlm.nih.gov/8165581/

Abstract
The theory of phase-shifting interferometry is not new but it is only recently, with the advent of solid-state detector arrays and fast image processors, that it has become a practical imaging technique. In conjunction with transmission interference microscopy, phase-shifting presents a new way of introducing contrast into the images of transparent microscopic objects such as cultured cells. An earlier paper from our laboratory has emphasised the advantages of transmission interference microscopy over phase contrast or differential interference contrast microscopy for the computerised analysis of cell behaviour. Phase-shifting greatly improves the accuracy, long-term stability and range of application of this technique but it has not previously, to our knowledge, been combined with transmission interference microscopy for the study of cultured cells. The resulting image is especially well suited to quantitative analysis by computer since it is a direct representation of the distribution of non-aqueous cellular material in the specimen. The image is not degraded by uneven illumination; by heterogeneous sensitivity of the detector array; or by differential absorption of light in the optics or specimen. Our main purpose in developing the method is to obtain sequences of images of the motile behaviour of cells in culture for analysis by computer. This type of analysis is potentially a powerful tool for studying the motile responses of cells and the operation and control of their locomotory machinery. Not only can the method be used for studying cell translocation and the dynamics of intracellular movement of non-aqueous material, but it is now possible to study in detail the time course of growth in individual cultured cells.

Author comments on publication IV (Dunn and Zicha, 1993)

The technique is based on a Leitz microscope (Figure 6).

Monochromatic light intensity, I, at each point of the CCD camera detector is given by the interference Equation

$$I = I_0(1 + \gamma \cos(\phi + \phi_0)) \tag{5}$$

where ϕ_0 is the background phase difference in radians between the object and reference beams, and this can be set to a known value by adjusting the microscope. The remaining three variables are unknown: I_0, the dc intensity; γ, the modulation or contrast of the interference fringes and ϕ, the additional phase difference introduced by the specimen. In the phase-stepping method, three images are acquired by incrementing ϕ_0 in steps of $\pi/2$ starting at $\pi/4$ by means of the motorized wedge compensator with intensities according to Equation 6, Equation 7, and Equation 8.

$$I_1 = I_0\left(1 + \gamma \cos\left(\phi + \frac{\pi}{4}\right)\right) \tag{6}$$

$$I_2 = I_0\left(1 + \gamma\cos\left(\phi + \frac{3\pi}{4}\right)\right) \quad (7)$$

$$I_3 = I_0\left(1 + \gamma\cos\left(\phi + \frac{5\pi}{4}\right)\right) \quad (8)$$

These equations can be solved for any of the three unknowns, and the solution for ϕ, which is usually the only one required, can be obtained from Equation 9 (Creath, 1988).

$$\tan(\phi) = (I_3 - I_2)/(I_1 - I_2) \quad (9)$$

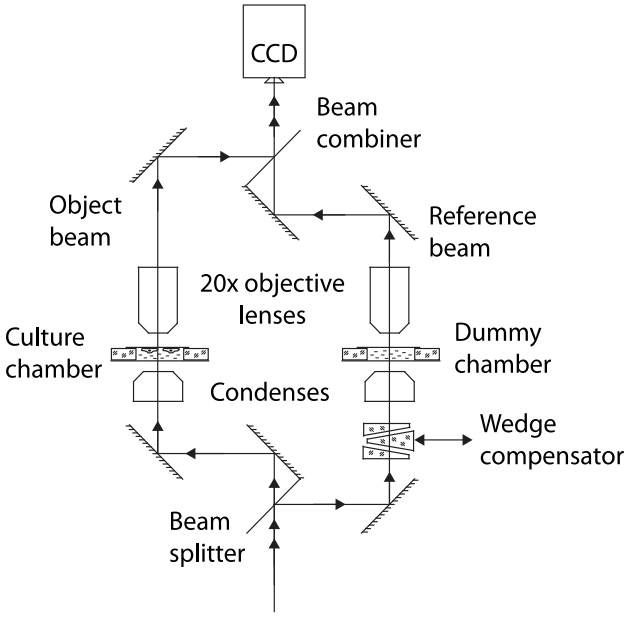

Figure 6. Optical diagram of the double-beam transmitted-light interference microscope according to Horn design.

The phase difference ϕ can be easily converted to the Optical Path Difference, *OPD*, in nm according to Equation

$$OPD = \frac{\phi\,\lambda}{2\pi} \quad (10)$$

where λ is the wavelength of an introduced LED light source (530 nm). Since the specific refractive index of all components of cells is similar, *OPD* can be expressed as Dry-Mass Density, *DMD*, using an average specific refractive index χ = 0.19, which is expressed per dry mass and volume according to Equation

$$DMD = OPD\,A/\chi \quad (11)$$

where *A* is the pixel area for *DMD* expressed as dry mass per pixel (Davies and Wilkins, 1952).

This technique provides an ultimate accuracy in the detection of the *DMD* of cells in tissue culture, routinely achieving *OPD* SEM of 2 nm.

Continuation of author comments on publication I (Zicha, 2022)

The Scientific Reports publication I introduced a better scientific CCD camera Orca ER (Hamamatsu) and software control implemented within the Micromanager image acquisition system (Edelstein et al., 2010). The phase shifting procedure was implemented as a Bash script

within the Micromanager system (presented in Appendix A). The phase shifting uses the continuous movement of the wedge compensator accurately synchronized with the burst mode image acquisition by the CCD camera, achieving the $\pi/2$ steps between individual corresponding points in subsequently acquired images, and Equation 9 can be used without modification.

The Scientific Reports publication I presents an improved DRIMAPS system, which was used to acquire time-lapse sequences with human carcinoma cells A549 in a control medium and treated with four anti-cancer drugs: an IGF1R inhibitor NVP-AEW541 (NVP), a PI3K inhibitor GDC0941 (GDC), a MEK inhibitor PD0325901 (PD), and another MEK inhibitor GSK1120212 (GSK). The time-lapse recordings lasted for 20 hours and used a 1-min lapse interval. The image sequences were processed by custom-developed software in Mathematica to calculate distributions of *OPD*. Further image processing was applied to remove fluctuations in the background, reconstruct the background, and subtract the reconstructed background. The image processing was based on a previously developed procedure published by the author (Zicha and Dunn, 1995).

3.1.5. Publication V: An image-processing system for cell behavior studies in subconfluent cultures

Zicha, D. and Dunn, G. A. (1995). *J. Microsc. Oxford* **179**, 11–21.

Open access link:
https://onlinelibrary.wiley.com/doi/abs/10.1111/j.1365-2818.1995.tb03609.x

Abstract
DRIMAPS (digitally recorded interference microscopy with automatic phase-shifting) is a system that we have developed for quantifying the behaviour of cells in subconfluent cultures. The primary data generated by the system consist of phase-shifted interference (PSI) images which are accurate density maps of the distribution of dry mass (non-aqueous material) inside cells. Time-lapse sequences of PSI images may be viewed as movie sequences or processed in various ways to reveal many different aspects of the dynamics of cell growth and motile behaviour. Here we describe the image processing routines that are an integral part of the system and are required for four main functions: 1 initial calculation of the PSI images; 2 compensation of these images for instrumental distortion and instability; 3 identification and tracking of individual cells to a time-lapse sequence of PSI Images; 4 extraction of cell behavioural data from a time-lapse sequence of PSI Images. The first function converts standard interference microscope images into an image that accurately represents the optical phase-difference introduced by the specimen. The second function recalibrates a sequence of images by taking the cell-free region in each image as a reference plane of zero phase-difference. This is particularly necessary to compensate for the long-term instability of the Horn type of double-beam interference microscope, which has several advantages over other types of interference microscope for studying cell behaviour. The third function compares consecutive images in a sequence in order to trace the identity of individual cells throughout the sequence. Semi-automatic tracking, which allows close interaction with a human operator, is less prone to error than fully automatic tracking. The fourth function automatically extracts dynamic data from the identified cells. These data may include the true mass centroids of cells for translocation analysis and robust morphometric parameters for cell morphology examination. The integrated intensity of a cell is an accurate measure of cell mass and allows the growth (increase in dry mass) of individual cells to be studied. These data may be entered into a relational database of cell behaviour and a rule-based system allows efficient data access and analysis. Experiments with phase-contrast microscopy have revealed that many of these

image processing methods are generally useful for cell behaviour studies using more conventional modes of microscopy.

Author comments on publication V (Zicha and Dunn, 1995)

The image processing system was based on background reconstruction, which uses the most frequent *OPD* values in time.

The subsequent segmentation was followed by the morphometry of cells, which was mainly based on the theory of moments. Two-dimensional moments were calculated according to Equation

$$m_{jk} = \sum x^j y^k f(x,y) \tag{12}$$

where *j* and *k* can be any non-negative integers, and the sum is taken over all the pixels in the image. The order of the moment is simply the sum *j+k*. For calculating the moments of the outline of an isolated cell, the function $f(x,y)$ is given a value of 0 if the pixel whose central coordinates are (x,y) lies outside the outline and 1 for the inside. For calculating the moments which take into account the dry-mass density (M_{jk}), the function $f(x,y)$ inside the cell is assigned the pixel value. The most useful moments include $m_{00,}$ which measures cell area, M_{00} is the total cell mass, and $\{M_{10}/M_{00}, M_{01}/M_{00}\}$are coordinates of the cell's center of gravity, the mass centroid, characterizing cell position.

Continuation of author comments on publication I (Zicha, 2022)

Areas covered by cells during the entire time-lapse do not feature dominant phase values representing the background. They are interpolated by a novel algorithm utilizing local values in the periphery of these areas and more global values in their centers, ensuring smooth features of the reconstructed background. Example images from a control sequence are in Figure 7. Subsequent cell segmentation newly allows the segmented cells to contain negative phase values, which is important to preserve accuracy in the thinnest parts of the cells.

The Total Cell Mass (*TCM*) and centroid positions are used for subsequent automatic cell tracking based on the nearest object with similar mass in the next frame. Protrusion dry mass, retraction dry mass, and dynamic polarity are then calculated based on the subtraction of subsequent frames.

Changes in the dry mass of cells and clusters were quantified as Dry-Mass Doubling Time (*DMDT*), which is evaluated for one object with *N* subsequent measurements of *TCM* according to Equation

$$DMDT = \frac{Ln(2)}{60 * Ln\left(1 + \frac{1}{(N-1)} \sum_{i=1}^{N-1} \left(\frac{TCM_{i+1}}{TCM_i} - 1\right)\right)} \tag{13}$$

where the coefficient of 60 converts the 1-min measurements to hours. The cell speed was calculated as the Euclidian distance of the centroid positions between subsequent frames multiplied by 60 to be expressed in μm h^{-1}. Protrusions and retractions were calculated from frame differences. Protrusion represents part of a cell that occupies new territory in the subsequent frame, and retraction is a part of a cell that occupies territory in the previous frame and is not occupied anymore in the subsequent frame. Dynamic polarity was evaluated as the distance between the protrusion centroid and the retraction centroid.

Dry-mass increase of individual cells and cell clusters was significantly (ANOVA $P < 0.02$) suppressed by GDC and less so by GSK. The mean value of dry-mass doubling time ± SEM was 22.1 ± 1.2 h and 30.4 ± 1.3 h for control and GDC cells, respectively. The speed of cell translocation was significantly (ANOVA $P < 0.04$) reduced only by GDC. The mean speed ± SEM of 17.0 ± 0.1 µm h^{-1} (N = 27 510) and 12.8 ± 1.2 µm h^{-1} (N = 27 012) was achieved by control cells and GDC-treated cells, respectively (Figure 8). The speed suppression can be mediated by a reduction in cell protrusion or dynamic polarity of protrusion/ retraction. In this case, the speed was suppressed mainly by a significant reduction of the dynamic cell polarity (ANOVA $P < 0.03$). The mean dynamic polarity ± SEM of 17.2 ± 0.8 µm (N = 27 510) and 16.9 ± 1.2 µm (N = 27 012) was achieved by control cells and GDC-treated cells, respectively. There were no significant changes in total protrusion mass, but the maximum mass value in the protrusion area was significantly reduced by the GDC treatment from 85 ± 2 femtograms (femtogram is 10^{-15} g) for control cells to 69 ± 2 femtograms, ANOVA $P < 0.05$. The GSK drug only partially reduced the growth with no effect on speed. The other two drugs NVP and PD did not achieve any significant changes in this test. GDC was thus identified as the best drug from the set for the A549 cells, significantly reducing growth as well as the speed by reducing dynamic polarity and maximum mass density in the protrusion area.

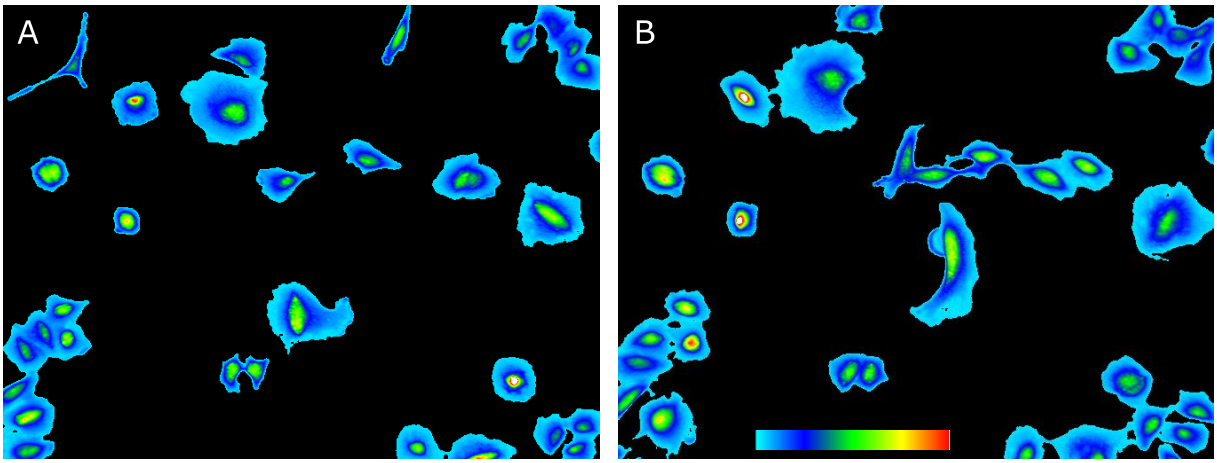

Figure 7. Example images from a time-lapse recording of A549 cells acquired by a Horn type Leitz double beam transmitted-light interference microscope equipped with a 20× twin objective lens and an Orca ER camera (Hamamatsu). The field size is 634 × 483 µm. (A) is a frame at time point 0 h, and (B) is a frame at time point 10 h. The pseudo-color bar represents a range of dry-mass densities from 0 to 1.6 pg µm^{-2}.

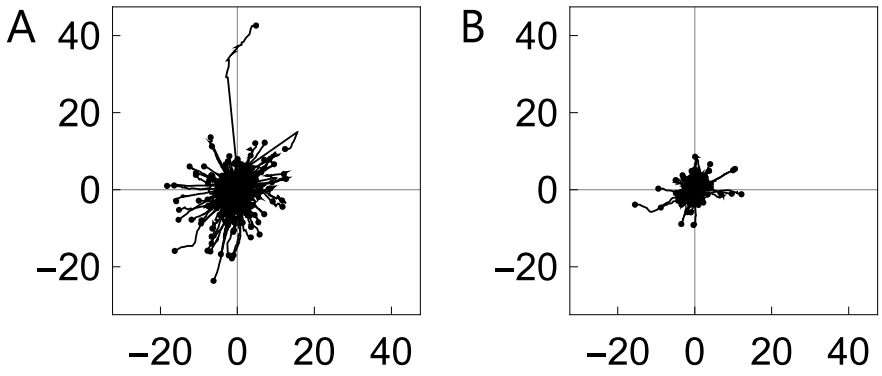

Figure 8. Rose plots of 30-min trajectories shifted with their starting point to the origin. A represents trajectories of control cells and B cells treated with GDC, illustrating its significant inhibition of cell motility. Axis x, y in µm.

The Horn design Leitz microscope has a fundamental setback since it is no longer commercially available. Moreover, it can only be used for one observation field at a time and does not combine with fluorescence. All these setbacks are resolved in a commercially available Q-Phase Microscope from Telight (Kolman and Chmelik, 2010; Slabý et al., 2010), which produces images comparable to the Horn design Leitz microscope since it is also a double-beam interference microscope with incoherent light source producing phase imaging which is free of coherence speckles and other artifacts. The Q-Phase operates in a holographic mode, and the phase-shifting procedure is not necessary. The optical thickness of cells is calculated from the holographic fringes using Fourier transforms. The exposure time is thus reduced to one camera frame, and faster processes can be observed. The Q-Phase system was used to characterize the motility and shape of leukemia cells (Seda et al., 2021).

3.1.6. Publication VI: FoxO1-GAB1 axis regulates homing capacity and tonic AKT activity in chronic lymphocytic leukemia

Seda, V., Vojackova, E., Ondrisova, L., Kostalova, L., Sharma, S., Loja, T., Pavlasova, G. M., Zicha, D., Peskova, M. K., Krivanek, J., Liskova, K., Kren, L., Benes, V., Litzmanova, K. M., Borsky, M., Oppelt, J., Verner, J., Pospisilova, S., Brychtova, Y., et al. (2021). *Blood* **138**, 758–772.

Open access link to full text:
https://www.ncbi.nlm.nih.gov/pmc/articles/PMC8513669/

Abstract
Recirculation of chronic lymphocytic leukemia (CLL) cells between the peripheral blood and lymphoid niches plays a critical role in disease pathophysiology, and inhibiting this process is one of the major mechanisms of action for B-cell receptor (BCR) inhibitors such as ibrutinib and idelalisib. Migration is a complex process guided by chemokine receptors and integrins. However, it remains largely unknown how CLL cells integrate multiple migratory signals while balancing survival in the peripheral blood and the decision to return to immune niches. Our study provided evidence that CXCR4/CD5 intraclonal subpopulations can be used to study the regulation of migration of CLL cells. We performed RNA profiling of $CXCR4^{dim}CD5^{bright}$ vs $CXCR4^{bright}CD5^{dim}$ CLL cells and identified differential expression of dozens of molecules with a putative function in cell migration. GRB2-associated binding protein 1 (GAB1) positively regulated CLL cell homing capacity of $CXCR4^{bright}CD5^{dim}$ cells. Gradual GAB1 accumulation in CLL cells outside immune niches was mediated by FoxO1-induced transcriptional GAB1 activation. Upregulation of GAB1 also played an important role in maintaining basal phosphatidylinositol 3-kinase (PI3K) activity and the "tonic" AKT phosphorylation required to sustain the survival of resting CLL B cells. This finding is important during ibrutinib therapy, because CLL cells induce the FoxO1-GAB1-pAKT axis, which represents an adaptation mechanism to the inability to home to immune niches. We have demonstrated that GAB1 can be targeted therapeutically by novel GAB1 inhibitors, alone or in combination with BTK inhibition. GAB1 inhibitors induce CLL cell apoptosis, impair cell migration, inhibit tonic or BCR-induced AKT phosphorylation, and block compensatory AKT activity during ibrutinib therapy.

Author comments on publication VI (Seda et al., 2021)

One of the aims of this publication was to identify the role of GAB1 protein function. The author contributed to the analysis of the Q-Phase time-lapse recordings. The recorded holograms were processed in Mathematica by in-house developed software, calculating the phase, which was followed by the processing described above in the case of the phase images derived from the Horn microscope recordings. Eliminating the GAB1 protein in leukemia cells, stimulated by medium conditioned with secretion products of stromal bone marrow, significantly reduced their 60-sec displacement from 3.75 ± 0.14 µm (control cells) to 2.71 ± 0.10 µm (mean ± SEM), ANOVA P-value < 0.035. When the cells were stimulated by a medium conditioned with secretion products of human mesenchymal stromal cells, the shape analysis revealed additional changes in *Elongation*, which was calculated from second-order moments (Alt, 1990) according to Equation

$$Elongation = 1 - \frac{b}{a} \tag{14}$$

where *a* and *b* are the long and short axis of elliptical shape approximation, respectively, calculated from orientation independent second-order moments *m*''' according to Equation 15 and Equation 16.

$$a = 2\sqrt{m'''_{20}} \tag{15}$$

$$b = 2\sqrt{m'''_{02}} \tag{16}$$

The rotation-independent moments *m*''' are calculated from normalized, size-independent moments, *m*'' according to Equations

$$m'''_{20} = m''_{20}cos^2(\varphi) + 2m''_{11}\sin(\varphi)\cos(\varphi) + m''_{02}sin^2(\varphi) \tag{17}$$

$$m'''_{02} = m''_{20}sin^2(\varphi) - 2m''_{11}\sin(\varphi)\cos(\varphi) + m''_{02}cos^2(\varphi) \tag{18}$$

where φ is the actual shape orientation (angle of the long axis) given by Equation

$$\tan(2\varphi) = 2m''_{11}/(m''_{20} - m''_{02}) \tag{19}$$

where the normalized moments *m*'' are calculated from centralized moments m' according to Equation 20, Equation 21, and Equation 22.

$$m''_{20} = m'_{20}/m_{00} \tag{20}$$

$$m''_{02} = m'_{02}/m_{00} \tag{21}$$

$$m''_{11} = m'_{11}/m_{00} \tag{22}$$

The centralized, position-independent moments m' are calculated from the second-order moments according to Equations

$$m'_{20} = m_{20} - m^2_{10}/m_{00} \tag{23}$$

$$m'_{02} = m_{02} - m^2_{10}/m_{00} \tag{24}$$

$$m'_{11} = m_{11} - m_{10}m_{01}/m_{00} \tag{25}$$

where m_{jk} are defined by Equation 12. Elongation of cells lacking GAB1 was significantly reduced from 0.317 ± 0.005 (control) to 0.296 ± 0.004 (mean ± SEM), ANOVA P-value < 0.027.

The results show the role of GAB1 in modulating shape and increasing cell motility which opens the possibility of targeting GAB1 by inhibitors to reduce leukemia invasion and metastasis.

3.2. Kindlin-3 protein in leukocyte cells

Leukocyte cells leave the bloodstream in response to inflammatory processes in the vicinity. Before they cross the blood vessel wall, they show rolling behavior while they are subjected to shear forces. The aim of this project was to elucidate the underlying molecular mechanism and to find the role of kindlin-3 protein in the rolling behavior relevant to leukocyte adhesion deficiency type III disorder (Willenbrock et al., 2013).

3.2.1. Publication VII: Novel automated tracking analysis of particles subjected to shear flow: Kindlin-3 role in B cells

Willenbrock, F., Zicha, D., Hoppe, A. and Hogg, N. (2013). *Biophys. J.* **105**, 1110–1122.

Open access link to full text:
https://www.sciencedirect.com/science/article/pii/S0006349513008448

Abstract
Shear flow assays are used to mimic the influence of physiological shear force in diverse situations such as leukocyte rolling and arrest on the vasculature, capture of nanoparticles, and bacterial adhesion. Analysis of such assays usually involves manual counting, is labor-intensive, and is subject to bias. We have developed the Leukotrack program that incorporates a novel (to our knowledge) segmentation routine capable of reliable detection of cells in phase contrast images. The program also automatically tracks rolling cells in addition to those that are more firmly attached and migrating in random directions. We demonstrate its use in the analysis of lymphocyte arrest mediated by one or more active conformations of the integrin LFA-1. Activation of LFA-1 is a multistep process that depends on several proteins including kindlin-3, the protein that is mutated in leukocyte adhesion deficiency-III patients. We find that the very first stage of LFA-1-mediated attaching is unable to proceed in the absence of kindlin-3. Our evidence indicates that kindlin-3-mediated high-affinity LFA-1 controls both the early transient integrin-dependent adhesions in addition to the final stable adhesions made under flow conditions.

Author comments on publication VII (Willenbrock et al., 2013)

In this co-authored publication, the author developed a flow chamber cell motility assay with advanced automatic tracking. The behavior of control leucocytes and leucocytes lacking kindling-3 protein was quantitatively compared. The cells were observed, and time-lapse was recorded in ibiTreat µ-slide VI channels (Ibidi) connected to a syringe pump to induce the shear flow. A Nikon Diaphot 300 microscope was used with a Sony XCD-X700 camera equipped with a 20× NA 0.4 phase contrast objective lens and AQM2001 Kinetic Acquisition Manager software (Kinetic Imaging Ltd., Bromborough, UK). The flow system was run for 3 min before recording was started, and then images were taken every second for 15 min. Videos from three separate areas of each flow chamber experiment were recorded.

The image segmentation step was introduced to identify cells in phase contrast images. As the first step, a 3×3 Prewitt filter was applied to enhance cellular features within the image. This was followed by an image segmentation approach based on scale-space image analysis. A scale-space image representation $I(x,y,s)$ with scale parameter s can be generated through convolving an image $I(x,y)$ with a Gaussian kernel where σ is a function of s, thus decreasing the scale with increasing σ and image structures, such as cells, get more blurred with increasing s and eventually diffuse totally into the background. The diffusion rate for each pixel position at each scale s can be extracted by calculating the intensity differential between images at subsequent scales $I(x,y,s)$ -

I(x,y,s+1), and areas with higher contrast will thus express higher diffusion rates. The background areas will result in low diffusion rates. Conversely, small debris diffuses quickly into the background and thus only initially expresses higher diffusion rates, while lighter or darker cellular regions produce higher positive diffusion rates over more scales. Our approach combines weighted positive diffusion rates over all *m* scales. Images at different scales are created by convolution with Gaussian kernels with σ=3×*s* applied to the enhanced image.

A global threshold *T* is applied to remove areas of non-uniform background as well as small debris, and cellular regions are subsequently identified using the connectivity principle. Centroid positions of the cellular regions are calculated and exported for the tracking procedure.

In order to track cell movement, the difference in trajectories of rolling cells was exploited, which move primarily in the direction of flow, compared to arrested and migrating cells, which migrate in random directions. Therefore, in contrast to the displacements of migrating cells, which fit a 2D circular Gaussian distribution, displacements of rolling cells are biased in the direction of the flow and fall within a probability distribution defined by a 2D elliptical Gaussian distribution with major axis aligned with the direction of flow according to Equation

$$f(x,y) = Ae^{-(a(x-x_0)^2+2b(x-x_0)(y-y_0)+c(y-y_0)^2)} \tag{26}$$

where *a*, *b* and *c* are defined by Equation 27, Equation 28, and Equation 29, respectively

$$a = \frac{cos^2\theta}{2\sigma_x^2} + \frac{sin^2\theta}{2\sigma_y^2} \tag{27}$$

$$b = \frac{-sin2\theta}{4\sigma_x^2} + \frac{sin2\theta}{4\sigma_y^2} \tag{28}$$

$$c = \frac{cos^2\theta}{2\sigma_y^2} + \frac{sin^2\theta}{2\sigma_x^2} \tag{29}$$

and *A* is the amplitude, x_0 and y_0 represent the center, σ_x and σ_y are measures of the spread of the distribution, and θ is the flow direction.

Both types of cell behavior could be tracked simultaneously by combining the normalized elliptical Gaussian distribution according to Equation

$$f'(x,y) = A'e^{-(a(x-x_0)^2+2b(x-x_0)(y-y_0)+c(y-y_0)^2)} \tag{30}$$

in which *A'* is the normalized amplitude, with the circular Gaussian to produce the penalty function *p*(*x*,*y*) according to Equation

$$p(x,y) = (x-x_0)^2 + (y-y_0)^2 - k({x_0}^2 + {y_0}^2)(f'(x,y) - 1) \tag{31}$$

where k is a constant determining the relative contribution of the elliptical Gaussian (Figure 9). This value is empirically determined and can be entered as an advanced parameter. The default value is 8, which was found to be optimal for the experimental conditions. Cell identity in the next frame is based on minimizing the penalty function.

B cells from LAD-III patients, which are mutated in the KINDLIN3 gene and lacking kindlin-3 protein, were found unable to roll slowly or attach firmly on LFA-1 ligand ICAM-1.

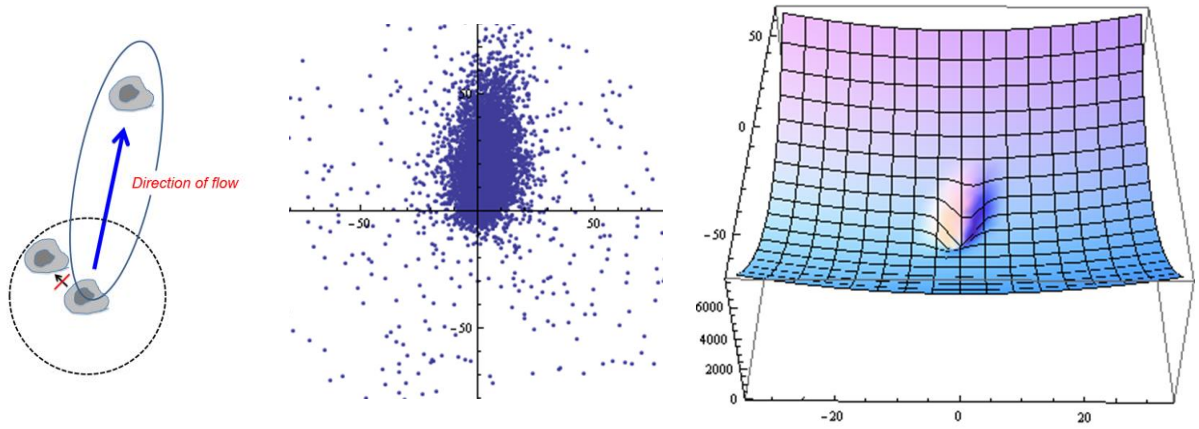

Figure 9. Illustration of biased tracking of cells under flow. The middle scatter plot contains all 1-sec displacements from a time-lapse recording, and the right-hand side penalty function was derived by fitting a 2D Gaussian to the density distribution of the scatter plot and adding a paraboloid to achieve an overall convex surface.

3.3. Novel biomarker for high content screening

The time-lapse analysis of cell motility provides detailed characterization but involves a time-consuming procedure. For screening purposes, it is sufficient to use faster and less accurate testing. The resulting hits of such a screen are subsequently confirmed by time-lapse. The author developed a novel indirect test for cell motility suitable for a special type of screening based on images with high information content (Zicha and Pardo, 2009).

3.3.1. Publication VIII: High content screening and analysis

Zicha, D. and Pardo, O. E. (2009). *Eur. Pharm. Rev.* **14**, 38–45.

Open access link to full text:
https://www.europeanpharmaceuticalreview.com/article/930/high-content-screening-and-analysis/

Abstract
High content screening (HCS) enables the discovery of novel regulators of biological and physiological processes in an unbiased manner using light microscopy imaging. It requires 1) a clearly identifiable phenotype with potential for regulation, 2) a collection of molecules, or library, to challenge this phenotype, 3) access to automation both at the experimental and image acquisition levels and 4) the technical means to perform subsequent high content analysis (HCA).

Author comments on publication VIII (Zicha and Pardo, 2009)

This first-author publication overviews High Content Screening (HCS) and introduces a novel end-point cell motility biomarker based on the Minimum Spanning Tree (MST). A MATLAB module was developed in-house (Appendix B) for the MST measurement using CellProfiler (Carpenter et al., 2006). Standard CellProfiler modules were first used to detect nuclei based on their DAPI stain, and cell bodies were detected in the surrounding space using F-actin stain and the watershed principle. Subsequently, the MST is calculated with the developed module, as illustrated in Figure 10. Distances are calculated between cell edges, and a set selected to connect all cells with the minimal total sum of the distances is selected using Prim's algorithm. This minimal total sum of the distances in the MST correlates with the speed of cell motility in

subconfluent cultures. The distances between edges correlate better than the distance between cell centers since this is the minimal distance that cells had to migrate after cell division.

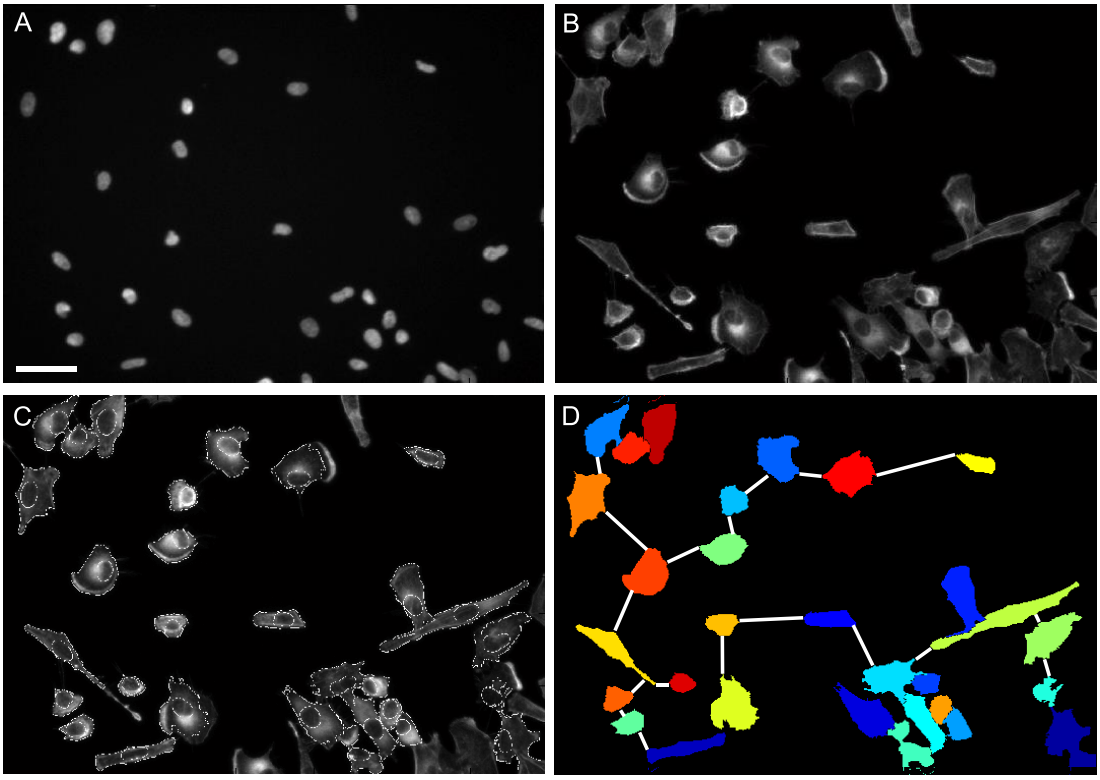

Figure 10. Example images of A549 cells acquired with the ImageXpress Micro HCS platform and illustration of processing with CellProfiler. Images of cell nuclei stained with DAPI (A) and F-actin stained with Phalloidin-Alexa Fluor 488 (B) were processed for the detection of nuclei and cell outlines (C) using the technique of watershed lines. Cell scattering is quantified by the Minimum Spanning Tree (MST), which is graphically represented (D) by white lines connecting all cells in the field while the sum of their lengths is minimal. Individual cells are color-coded. The scale bar is 50 µm.

3.4. Ephrin-B2 protein in vascular smooth muscle cells

Important aspects of the behavior of vascular smooth muscle cells in development are their motility and spreading (Foo et al., 2006).

3.4.1. Publication IX: Ephrin-B2 controls cell motility and adhesion during blood-vessel-wall assembly

Foo, S. S., Turner, C. J., Adams, S., Compagni, A., Aubyn, D., Kogata, N., Lindblom, P., Shani, M., Zicha, D. and Adams, R. H. (2006). *Cell* **124**, 161–173.

Open access link to full text:
https://www.sciencedirect.com/science/article/pii/S0092867405012341

Abstract

New blood vessels are initially formed through the assembly or sprouting of endothelial cells, but the recruitment of supporting pericytes and vascular smooth muscle cells (mural cells) ensures the formation of a mature and stable vascular network. Defective mural-cell coverage is associated with the poorly organized and leaky vasculature seen in tumors or other human diseases. Here we

report that mural cells require ephrin-B2, a ligand for Eph receptor tyrosine kinases, for normal association with small diameter blood vessels (microvessels). Tissue-specific mutant mice display perinatal lethality; vascular defects in skin, lung, gastrointestinal tract, and kidney glomeruli; and abnormal migration of smooth muscle cells to lymphatic capillaries. Cultured ephrin-B2-deficient smooth muscle cells are defective in spreading, focal-adhesion formation, and polarized migration and show increased motility. Our results indicate that the role of ephrin-B2 and EphB receptors in these processes involves Crk-p130(CAS) signaling and suggest that ephrin-B2 has some cell-cell-contact-independent functions.

Author comments on publication IX (Foo et al., 2006)

In this co-author publication, which received 330 citations, the author contributed with analysis of cell motility, used a robotized high-content screening system, and developed automated analysis for cell spreading. The image processing required for the cell spreading analysis was implemented in Metamorph as a Journal (Figure 11). Control vascular smooth muscle cells and cells without ephrin-B2 protein were cultured, fixed, stained, and imaged with the Discovery 1 high-content screening system (Figure 11 F). The Metamorph Journal used the segmented cells and calculated *ShapeFactor* of the cells according to Equation

$$ShapeFactor = \frac{4\pi Area}{Perimenter^2} \tag{32}$$

where *Area* is the cell spread area and *Perimeter* is the length of the cell outline. The *ShapeFactor* of the cells without ephrin-B2 protein was significantly reduced to 0.24 ± 0.007 (mean ± SEM) while the control cells had 0.30 ± 0.008, ANOVA $P < 0.03$, degrees of freedom were 1 for treatment, 4 for experiments, 41 for coverslips, 376 for observation sites and 7839 for individual cells. This reduction reflects the increased complexity of the cell shape, which is required for their increased motility.

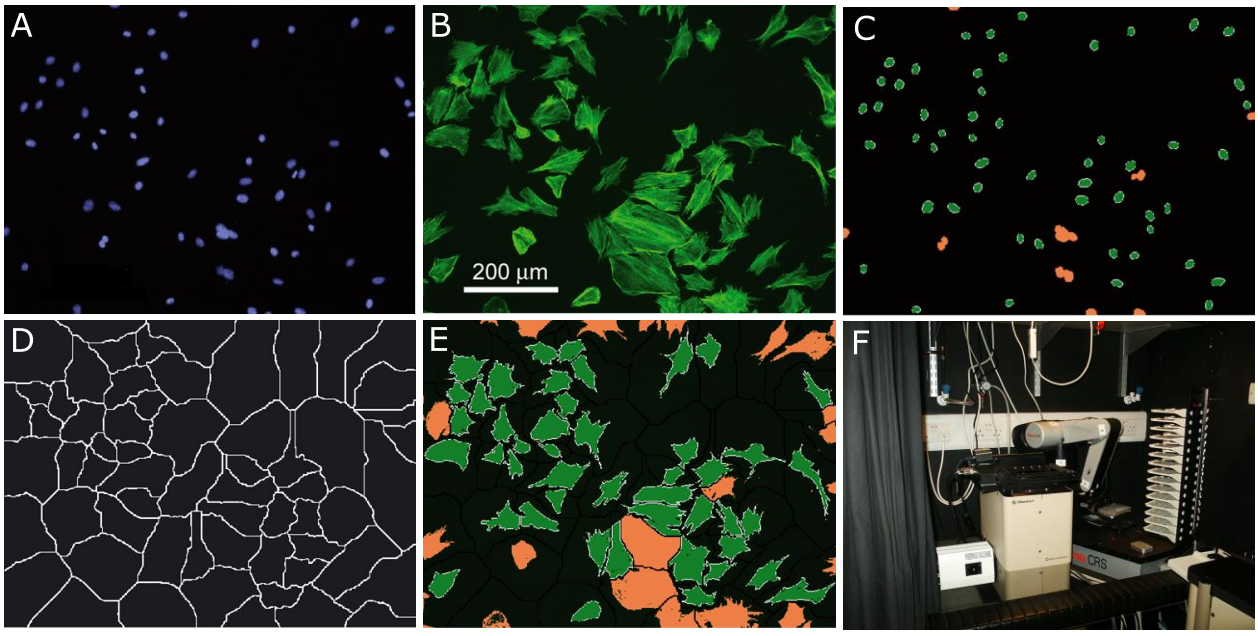

Figure 11. Imaging of vascular smooth muscle cells. (A) Image of DAPI stained nuclei. (B) Image of F-actin labeled with Alexa Fluor 488 phalloidin. Images were acquired with an S fluor 20× NA 0.75 Nikon objective lens. (C) Segmented nuclei (green) with clusters rejected on size (orange). (D) Watershed lines around segmented nuclei using intensity distribution in B. (E)

Segmented cells based on the watershed lines (green) and rejected cells (orange) based on rejected nuclei and touching border. (F) High content screening system Discovery 1 (Molecular Devices).

3.5. Chemotaxis

Directional migration, chemotaxis, is an important biological process with roles in development, inflammatory responses, and cancer (Jin et al., 2008; Zicha et al., 1991).

3.5.1. Publication X: A new direct-viewing chemotaxis chamber

Zicha, D., Dunn, G. A. and Brown, A. F. (1991). *J. Cell Sci.* **99**, 769–775.

Open access link to full text:
http://jcs.biologists.org/content/99/4/769

Abstract

A new form of chamber for studying chemotaxis, similar in principle to the Zigmond chamber, allows the behaviour of the cells in a linear concentration gradient to be observed directly. The chamber was developed mainly for studying chemotaxis in fibroblasts using interferometric microscopy and the main design criteria were that it should have better optical characteristics, a higher dimensional precision and better long-term stability than the Zigmond chamber. It is made entirely from glass by grinding a blind circular well centrally in the counting platform of a Helber bacteria counting chamber. This procedure leaves an annular 'bridge', approximately l mm wide, between the new inner circular well and the original outer annular well. This bridge fulfils the same function as the linear bridge of the Zigmond chamber but the precise construction of the counting chamber ensures that a gap of 20 µm between bridge and coverslip can be accurately and repeatedly achieved when the chamber is assembled. It is envisaged that the improved optical clarity, dimensional accuracy and long-term stability of the new chamber will be advantageous in other applications, particularly in studies requiring critical microscopy or a precise knowledge of the gradient and in studies of cells, such as fibroblasts, that move much more slowly than neutrophils.

Author comments on publication X (Zicha et al., 1991)

This first-author publication on the development of a new chemotaxis chamber has received 289 citations. The paper describes the design, construction, and first application of the direct-viewing glass chamber with unprecedented stability of the chemotactic gradient. The stability is based on a circular arrangement with two concentric wells (Figure 12) where the center well is blind, which prevents any flow. The first prototype was produced in-house by modification of a bacteriological counting chamber without grating. Outer dimensions 75 mm × 25 mm × 1 mm were identical to a standard slide, and the central circular island was polished 20 µm below the surrounding surface by the manufacturer. The central well was additionally excavated by a diamond burr. The chamber was designed by the second co-author of this publication and is now commercially available from Weber Scientific as the Dunn chemotaxis chamber.

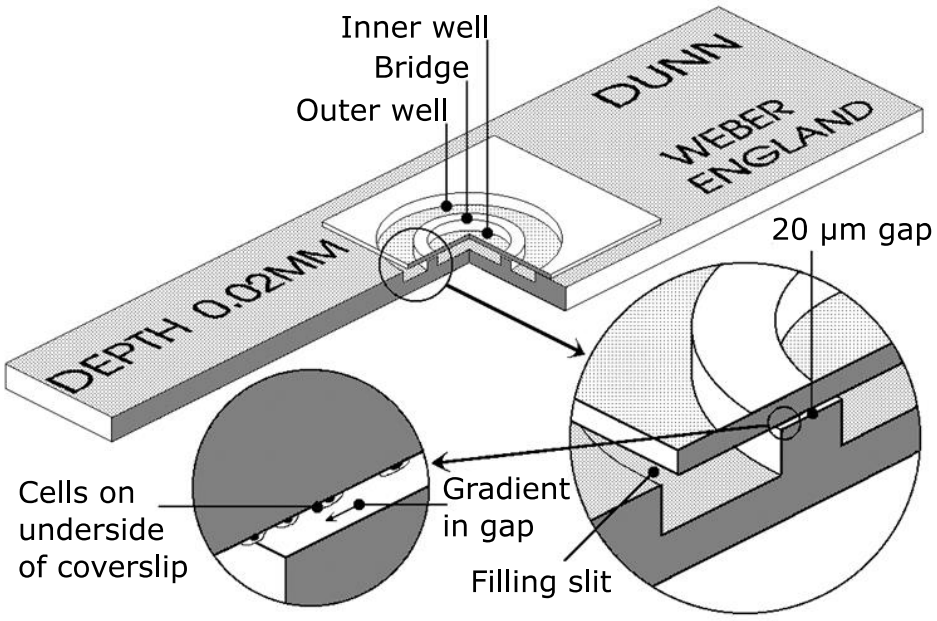

Figure 12. Drawing of the chemotaxis chamber.

The diffusion in the 20 µm bridge region is theoretically equivalent to diffusion in a hollow cylinder, and solutions for the steady and non-steady situations were derived by Crank in 1956 (Crank, 1975). In the steady state, the concentration *C* as a function of distance, *r*, from the center of the chamber is given by Equation

$$C(r) = \frac{C_i \ln\left(\frac{b}{r}\right) + C_o \ln\left(\frac{r}{a}\right)}{\ln\left(\frac{b}{a}\right)} \tag{33}$$

where C_i and C_o are the concentrations of the chemotactic agent per volume in the inner and outer wells, respectively, and *a* and *b* are the inner and outer radii of the bridge. The gradient is not strictly linear, but with the small dimensions of the bridge region, the deviation from linearity is minimal. If the inner well and the bridge region have initial concentrations of zero, the concentration profile as a function of time, *t*, for a molecule with a diffusion coefficient, *D*, is given by Equation

$$C(r,t) = \frac{C_o \ln(\frac{r}{a})}{\ln(\frac{b}{a})} - \pi \sum_{n=1}^{\infty} \frac{C_o U_0(r\alpha_n)}{1 - \frac{J_0^2(b\alpha_n)}{J_0^2(a\alpha_n)}} e^{-D\alpha_n^2 t} \tag{34}$$

where

$$U_0(r\alpha_n) = J_0(r\alpha_n)Y_0(b\alpha_n) - J_0(b\alpha_n)Y_0(r\alpha_n) \tag{35}$$

and the α_n values are the positive roots of Equation 36.

$$U_0(a\alpha_n) = 0 \tag{36}$$

The measured formation of the gradient in the chamber closely followed the theoretical formation (Figure 13). The initial discrepancy at the high concentration end resulted from the meniscus

formed by the control medium before the outer well was filled with a medium containing the rhodamine/dextran dye.

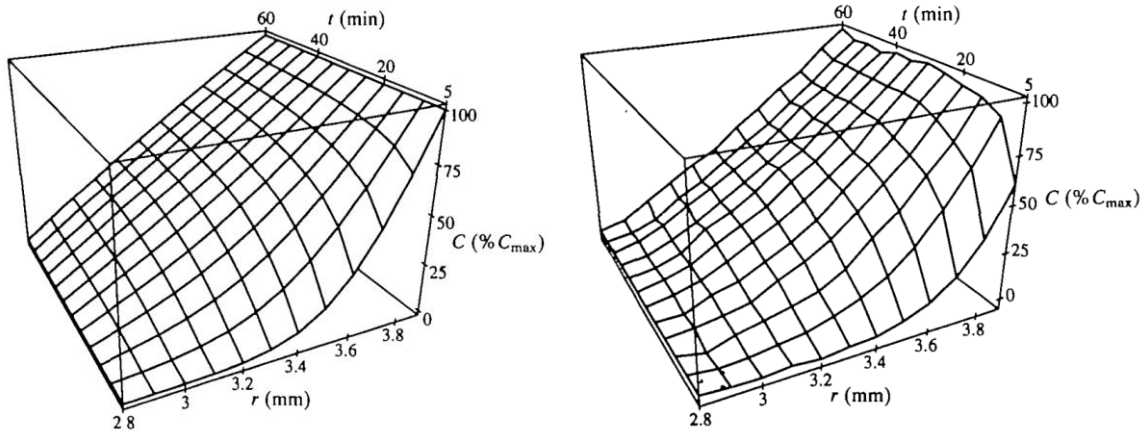

Figure 13. Theoretical (left) and measured gradient formation in the chamber (right). The theoretical formation was calculated according to Equation 34 with a hypothetical chemotactic factor with a diffusion coefficient of 13.3×10^{-5} mm^2 s^{-1}. The measurement used rhodamine/dextran dye and its amount Q was determined in relative terms as fluorescence intensity by a CCD camera.

Equation 34 is only valid if the concentrations in the two wells remain constant during time *t*. For the actual dimensions of the chamber, this is a very good approximation during the approach to the steady-state condition, but estimating the long-term decay of the gradient requires taking into account the flux across the bridge and the subsequent changes in the concentrations of the wells. Since very little of the total material passes from the outer to the inner well during the approach to the steady state, it is adequate to consider only the steady-state flux. The flux of diffusing substance, d*Q*/d*t*, from outer to inner well through the gap of height *h* over the bridge is given by Equation

$$\frac{dQ}{dt} = \frac{2\pi hD(C_\mathrm{o} - C_\mathrm{i})}{\ln(\frac{b}{a})} \tag{37}$$

which can be written as a first-order differential equation in terms of the steady-state gradient $G(t)=(C_o-C_i)/(b-a)$ and solved to give Equation

$$G(t) = G(0)e^{-kDt} \tag{38}$$

where

$$k = \frac{2\pi h(v_i + v_o)}{\ln(\frac{b}{a})v_i v_\mathrm{o}} \tag{39}$$

and v_i and v_o are the volumes of the inner and outer wells.

Theoretical decay compares well with the long-term measured decay (Figure 14). There was a detectable gradient after the 96 h.

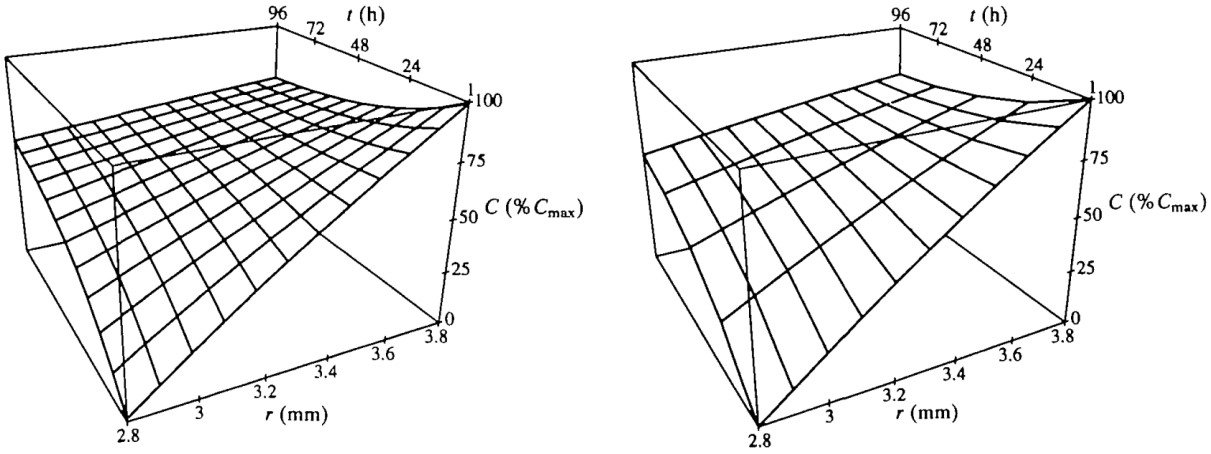

Figure 14. Theoretical (left) and measured (right) decay of the gradient. The hypothetical factor and dye are identical to Figure 13, v_i = 14 µl, v_o = 20 µl, and h = 0.02 mm.

The chamber was subsequently used to analyze the chemotaxis of macrophages in Wiskott-Aldrich syndrome patients (Zicha et al., 1998).

3.5.2. Publication XI: Chemotaxis of macrophages is abolished in the Wiskott-Aldrich syndrome

Zicha, D., Allen, W. E., Brickell, P. M., Kinnon, C., Dunn, G. A., Jones, G. E. and Thrasher, A. J. (1998). *Br J Haematol* **101**, 659–665.

Open access link to full text:
https://onlinelibrary.wiley.com/doi/full/10.1046/j.1365-2141.1998.00767.x

Abstract
Wiskott-Aldrich syndrome (WAS) is a rare disease characterized by microthrombocytopenia, eczema and immune deficiency. In this study a direct-viewing chemotaxis chamber was used to analyse chemotactic responses of WAS neutrophils and macrophages in stable linear concentration gradients. In five patients with classic WAS, chemotaxis of macrophages but not of neutrophils was found to be abolished, whereas the speed of random motility of both cell types was found to be indistinguishable from control cells. This supports the existence of an essential functional link, previously suggested by biochemical studies, between Cdc42, WAS protein (WASp) and the actin cytoskeleton in primary human macrophages. Moreover, these data suggest that Cdc42-WASp-mediated filopodial extension is a requirement for chemotaxis but not for chemokinesis in these cells. Abnormal directional cell motility of macrophages and related antigen-presenting cells may play a significant part in the immune deficiency and eczema of WAS.

Author comments on publication XI (Zicha et al., 1998)

Neutrophils and mononuclear cells were isolated from the peripheral blood of control healthy subjects and male patients with severe Wiskott-Aldrich syndrome (WAS). Neutrophils were tested in gradients of their standard chemoattractant FMLP. The mononuclear cells were differentiated into macrophages and exposed to CSF-1 gradients. The motility of the cells was recorded by time-lapse microscopy, and cell trajectories were interactively tracked. Example trajectories of WAS neutrophils and macrophages are shown in Figure 15. In order to statistically evaluate their chemotactic response, the trajectories were converted to directions.

The direction of a trajectory is the angle at which the cell reaches a chosen arbitrary horizon distance. Non-motile cells, which never reach the horizon distance, are automatically precluded from the analysis. This is a desirable feature because chemotaxis is defined for translocating cells only. A conversion including n cells translocating more than the horizon distance generates a set of directions θ_1, $\theta_{2, \ldots,}$ θ_n. The developed Mathematica program for evaluation of the directionality, based on statistics of directional data (Mardia, 1975), then calculates the mean direction, $\bar{D}$, from Equation

$$\tan(\bar{D}) = \bar{S}/\bar{C} \tag{40}$$

where $\bar{S}$ and $\bar{C}$ are defined by Equation 41 and Equation 42, respectively.

$$\bar{S} = 1/n \sum \sin(\theta_i) \tag{41}$$

$$\bar{C} = 1/n \sum \cos(\theta_i) \tag{42}$$

The mean resultant length, $\bar{R}$, is then calculated from Equation 43.

$$\bar{R} = (\bar{C}^2 + \bar{S}^2)^{1/2} \tag{43}$$

The Rayleigh test for unimodal clustering of directions provides a P-value using the mean resultant length, $\bar{R}$. If the null hypothesis about the uniform distribution is rejected by the Raleigh test ($p<0.01$ or $p<0.05$), then a conclusion can be accepted that the cells are showing a significant directional response and the 99% or 95% confidence interval of the mean direction, $\bar{D}$, can be determined on the basis of *n* and $\bar{R}$. In order to confirm that the response is chemotaxis to the known gradient, however, it should also be demonstrated that the direction of the gradient lies within the confidence interval of the mean cell direction $\bar{D}$.

The results of the statistical analysis are shown in Figure 16. WAS neutrophils show a strong chemotactic response, similar to normal control macrophages, while chemotaxis in WAS macrophages is abrogated.

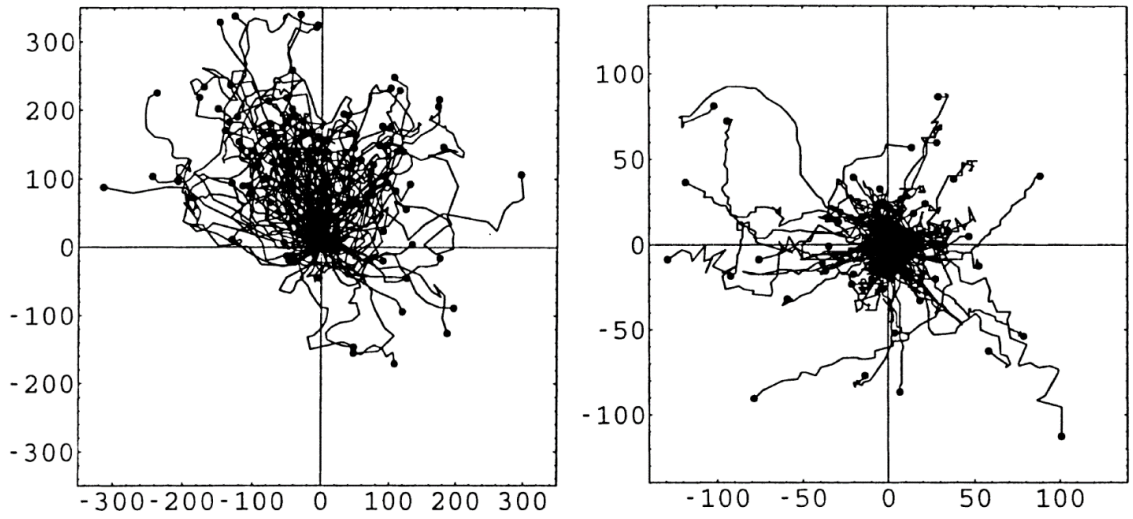

Figure 15. Comparison of WAS neutrophil and macrophage trajectories. Trajectories of WAS neutrophil leucocytes in gradients of FMLP (left) and trajectories of WAS macrophages in gradients of CSF-1 (right). Each plot shows a sample of the 100 longest trajectories from pooled data. All trajectories were shifted with their starting point to the origin. Axes are labeled in µm, and the track duration is up to 1 h for neutrophil leucocytes and up to 4 h for macrophages. The gradient direction is upwards.

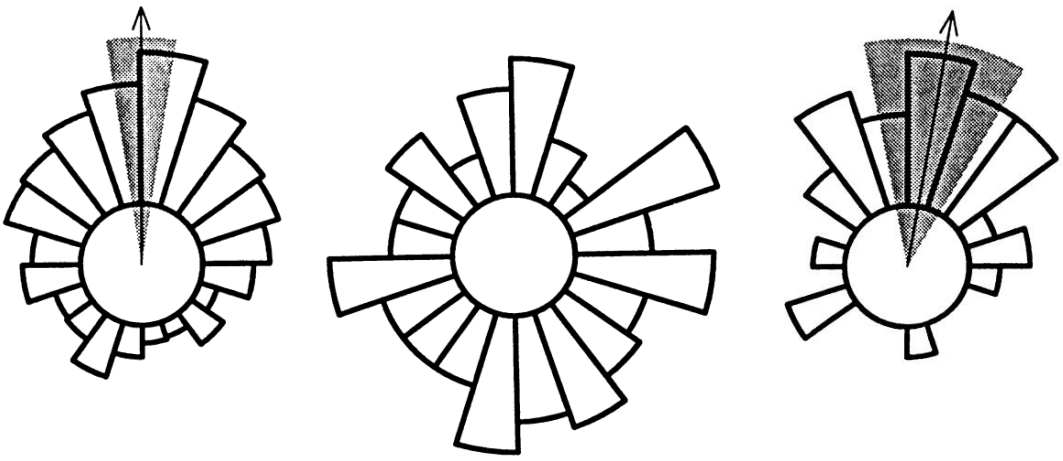

Figure 16. Chemotaxis of neutrophils and macrophages. Circular histogram of neutrophil directions in gradients of FMLP from WAS patients (left). The sample size n was 564 cells, and the Rayleigh test P-value < 0.00001. The P-value indicates significant clustering of neutrophil directions around the gradient direction (upwards) and therefore demonstrates positive chemotaxis of the WAS neutrophils. Circular histograms of macrophage directions in gradients of CSF-1 from control subjects (right) and WAS patients (middle). The sample size (n) and Rayleigh test P-value were n = 30 and P < 0.00001 for control subjects, and n = 121 and P = 0.50 for WAS patients. The gradient direction is upwards, and the P-values indicate significant positive chemotaxis for macrophages from control subjects, but there is no preferred directionality for macrophages from WAS patients. Arrows represent the mean directions, and grey wedges 99% confidence intervals in cases of significant unimodal clustering of directions.

The author subsequently rescued the chemotaxis defect in Wiskott-Aldrich syndrome macrophages by reintroducing the missing protein (Jones et al., 2002).

3.5.3. Publication XII: Restoration of podosomes and chemotaxis in Wiskott-Aldrich syndrome macrophages following induced expression of WASp

Jones, G. E., Zicha, D., Dunn, G. A., Blundell, M. and Thrasher, A. (2002). *Int J Biochem Cell Biol* **34**, 806–815.

Open access link to full text:
https://www.sciencedirect.com/science/article/pii/S1357272501001625

Abstract
We used a direct-viewing (Dunn) chemotaxis chamber to analyse the chemotactic responses of human normal and Wiskott–Aldrich syndrome (WAS) macrophages to the cytokine colony stimulating factor-1 (CSF-1). In five patients with classic WAS, where specialised adhesion complexes called podosomes are absent, chemotaxis of macrophages was abolished. The deficient chemotactic responses of WAS macrophages following cytokine stimulation could be correlated with abnormalities in cell polarisation and actin organisation. In a series of cell microinjection studies we found that normal chemotactic responses were restored in WASp macrophages transfected with a full-length human WAS construct. Expression of exogenous WAS protein (WASp) in these cells also restored normal polarised cell morphology and the ability to form podosomes.

Author comments on publication XII (Jones et al., 2002)

The two publications identified the mechanism of the Wiskott-Aldrich syndrome, where the immune deficiency is mediated by the abrogated chemotaxis of macrophages due to the mutant WASp protein, while the chemotaxis of neutrophils is not affected (Figure 16 and Figure 17).

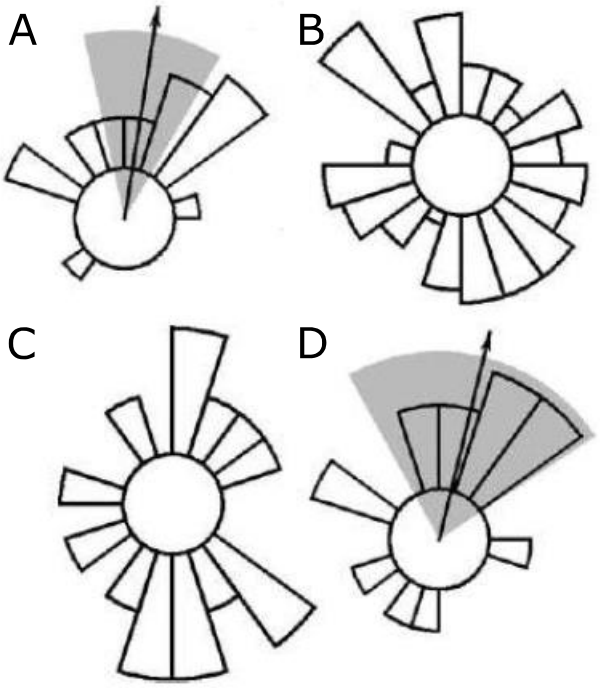

Figure 17. Analysis of directions of cell trajectories in response to a gradient of the chemoattractant (CSF-1, source at 36 ng/ml). In each case, the horizon distance was chosen as the largest distance reached by 70% of the cells. In cases where a significant clustering of directions has occurred, the mean direction is indicated by an arrow and its 95% confidence interval by a grey sector. Non-injected macrophages were of normal type, showing chemotaxis (A) and WAS type, with abrogated chemotaxis (B). WAS macrophages were also induced to express EGFP only as a control by microinjection with a transfection vector (C) or EGFP + WASp protein recovering the chemotaxis (D). The chemotaxis rescue is an unequivocal prove that the abrogated chemotaxis in WAS is due to the missing WASp protein.

4. INTRACELLULAR MOTION AND CHARACTERISATION OF MOLECULES

Additional developments of the author in light microscopy techniques were focused on intracellular and molecular measurements complementing the cell motility studies and addressing the role of mutant connexin 31 proteins and their interactions in diseases and characterizing a transfection vector. The transfection vectors contain DNA and are used to introduce additional proteins inti cells as a defined experimental treatment.

4.1. Role of mutant connexin 31 proteins

Similar mutations in the connexin 31 protein determine entirely different diseases, namely related to skin and neuropathy/hearing loss (Abrams et al., 2006). Since connexin 31 is known to be involved in cell-to-cell communication, the hearing deficiency is understandable as signals from the ear must be communicated to the brain. The involvement in skin diseases was puzzling, and the author contributed to the elucidation of the mechanism. Here, the problem is not directly related to cell-to-cell communication but to the unhealthy accumulation of the mutant non-functional protein in cells leading to their stress and subsequent death (Tattersall et al., 2009).

4.1.1. Publication XIII: EKV mutant connexin 31 associated cell death is mediated by ER stress

Tattersall, D., Scott, C. A., Gray, C., Zicha, D. and Kelsell, D. P. (2009). *Hum Mol Genet* **18**, 4734–4745.

Open access link to full text:
https://academic.oup.com/hmg/article/18/24/4734/581216

Abstract
The epidermis expresses a number of connexin (Cx) proteins that are implicated in gap junction-mediated cell communication. Distinct dominantly inherited mutations in Cx31 cause the skin disease erythrokeratoderma variabilis (EKV) and hearing loss with or without neuropathy. Functional studies reveal tissue-specific effects of these Cx31 disease-associated mutations. The Cx31 mutants (R42P)Cx31, (C86S)Cx31 and (G12D)Cx31 are associated with EKV and the mutant (66delD)Cx31 with peripheral neuropathy and hearing loss, however the mechanisms of pathogenesis remain to be elucidated. Expression of (R42P)Cx31, (C86S)Cx31 and (G12D)Cx31 *in vitro*, but not (WT)Cx31 or (66delD)Cx31, cause elevated levels of cell-type specific cell death. Previous studies suggest that Cx-associated cell death may be related to abnormal 'leaky' hemichannels but we produced direct evidence against that being the major mechanism. Additionally, our immunocytochemistry showed upregulation of components of the unfolded protein response (UPR) in cells expressing the EKV-associated Cx31 mutants but not (WT)Cx31 or (66delD)Cx31. We conclude that the endoplasmic reticulum (ER) stress leading to the UPR is the main mechanism of mutant Cx31-associated cell death. These results indicate that, *in vivo*, ER stress may lead to abnormal keratinocyte differentiation and hyperproliferation in EKV patient skin.

Author comments on publication XIII (Tattersall et al., 2009)

In this co-author publication, the author used a method for quantifying intercellular communication, which he developed previously (Di et al., 2002), and a novel assessment of cell

death. The results allowed us to discover the mechanism of the skin disease erythrokeratoderma variabilis linked to connexin 31 mutations. Connexin 31 is involved in cell-cell communication. Here its mutation, however, induces cell death leading to the skin defect.

In order to prove that the cell death was not a consequence of aberrantly formed channels with the mutant protein, the publication introduced a combined test visualizing calcium and intracellular motility. Timing measurements showed that the intracellular activity seized well before the cell lost its calcium after the cell death (Figure 18). The cell death, therefore, could not have been caused by the loss of calcium through aberrant communication channels.

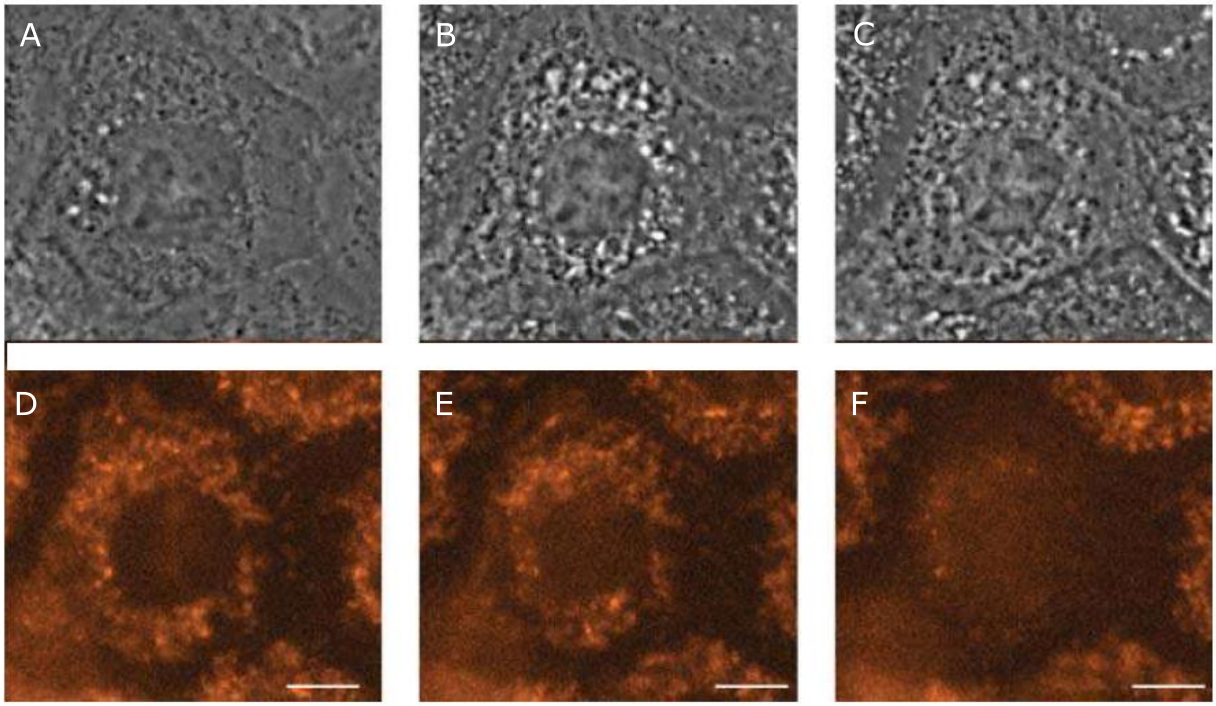

Figure 18. Calcium indicator (Calcium Orange) does not leave the cells expressing EKV-associated Cx31, while they are undergoing cell death, eliminating a hemichannel mechanism. Examples of images from time-lapse recording of keratinocytes expressing (G12D)Cx31-EGFP which was induced by microinjection with an expression vector. Although EGFP was also recorded, only phase contrast (A, B and C) and Calcium Orange images (D, E and F) are presented. Cells were loaded with Calcium Orange 30 min after microinjection and recording started 50 min after microinjection. The cell in the centre of the field starts dying 73 min after microinjection (A and D), died 81 min after microinjection (B and E) and lost calcium 85 min after microinjection (C and F). Scale bars are 10 μm.

4.1.2. Publication XIV: Defective trafficking and cell death is characteristic of skin disease-associated connexin 31 mutations

Di, W. L., Monypenny, J., Common, J. E., Kennedy, C. T., Holland, K. A., Leigh, I. M., Rugg, E. L., Zicha, D. and Kelsell, D. P. (2002). *Hum Mol Genet* **11**, 2005–2014.

Open access link to full text:
https://academic.oup.com/hmg/article/11/17/2005/589972

Abstract
Distinct germline mutations in the gene (GJB3) encoding connexin 31 (Cx31) underlie the skin disease erythrokeratoderma variabilis (EKV) or sensorineural hearing loss with/without peripheral

neuropathy. Here we describe a number of functional analyses to investigate the effect of these different disease-associated Cx31 mutants on connexon trafficking and intercellular communication. Immunostaining of a biopsy taken from an EKV patient harbouring the R42P mutation revealed sparse epidermal staining of Cx31, and, when present, it had a perinuclear localization. Transfection and microinjection studies in both keratinocytes and fibroblast cell lines also demonstrated that R42P and four other EKV-associated mutant Cx31 proteins displayed defective trafficking to the plasma membrane. The deafness/neuropathy only mutant 66delD had primarily a cytoplasmic localization, but some protein was visualized at the plasma membrane in a few transfected cells. Both 66delD- and R32W-Cx31/EGFP proteins had significantly impaired dye transfer rates compared to wild-type Cx31/EGFP protein. A striking characteristic feature observed with the dominant skin disease Cx31 mutations was a high incidence of cell death. This was not observed with wild-type, R32W 66delD Cx31 proteins. In conclusion, we have identified some key cellular phenotypic differences with respect to disease-associated Cx31 mutations.

Author comments on publication XIV (Di et al., 2002)

In order to quantify intercellular communication, the author developed a procedure that measures the spread of a small dye from a cell to the adjacent cells. The dye, Alexa Fluor 568, was chosen since it passes through the intercellular channels formed by the protein of interest – connexin 31. Example images from the experiments are presented in Figure 19.

Images were acquired every 20 s in three separate channels: phase contrast, Green Fluorescent Protein (GFP) fluorescence, and Alexa Fluor 568 fluorescence; using a 20× NA 0.5 objective lens, an Orca ER scientific CCD camera (Hamamatsu), and a multiple dichroic mirror in conjunction with motorized excitation and emission filter wheels (Sutter Instruments). Image acquisition was controlled using Acquisition Manager (Kinetic Imaging). The exposure time for the Alexa Fluor 568 channel was kept constant between all time-lapse experiments. The microscope body was housed in a Perspex environment chamber accurately maintained at 37°C and the cells were enclosed within a glass-topped, steel humidity chamber upon completion of cytoplasmic microinjection. The time elapsed from the microinjection of dye to the commencement of image acquisition was approximately one minute. Fluorescence images of the Alexa Fluor 568 dye were cropped, binned to a pixel size of 2.6 × 2.6 μm, and automatically thresholded. The site of dye microinjection was interactively marked using a mouse pointer, and the Normalized Mean Distance (*NMD*) of dye transfer was calculated for each frame in the sequence according to Equation

$$NMD(t) = \sum I_{xy}(t) d_{xy}(t) \,/\, \sum I_{xy}(t) \qquad (44)$$

where $I_{xy}(t)$ is the intensity of an image pixel (x, y) at time t, and $d_{xy}(t)$ is the distance of the pixel (x, y) from the site of dye microinjection. $NMD(t)$ data evaluated for the initial 10 min of a recording were subjected to a linear regression analysis, and the slope of the regression function was taken as the rate of the dye transfer for the particular sequence. The significances of differences in the rate of the dye transfer between groups of sequences were evaluated by a two-sided t-test. Image processing, regression analysis, and statistical tests were performed in Mathematica (Wolfram Research) using specially developed software. The mean rate of the dye transfer was significantly reduced in cells with the mutation linked to deafness/neuropathy, achieving mean ± SEM of 3.47 ± 0.65 μm/h (8 movies) compared to wild-type protein 10.06 ± 1.92 μm/h (10 movies) with P-value < 0.01.

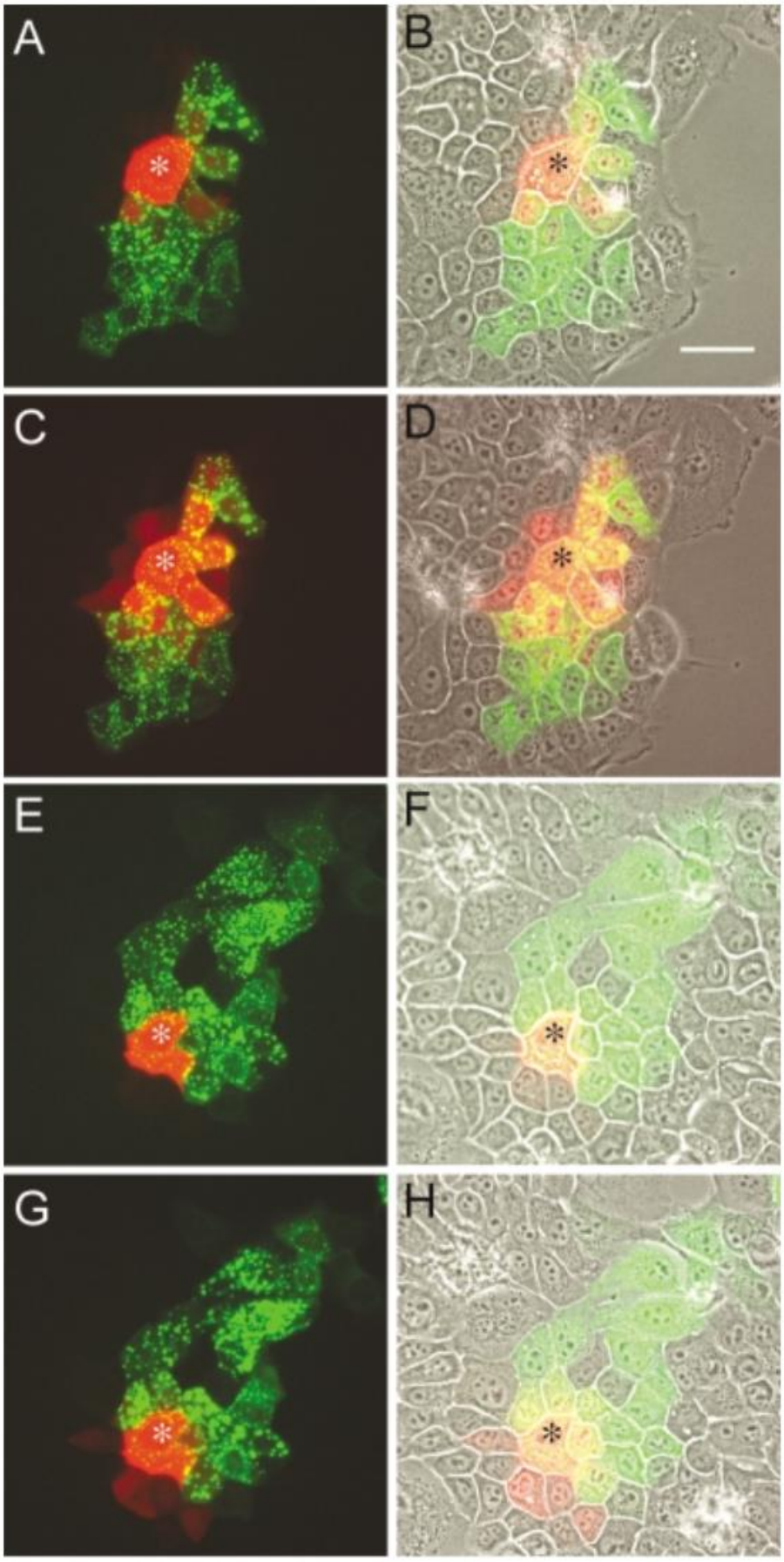

Figure 19. Dye transfer analysis using Alexa Fluor 658 in skin cells after introduction of connexin 31 protein fused to GFP. The left column presents an overlay of the red (Alexa Fluor 658 dye) and green fluorescence (GFP) channels, and the right column is additionally overlaid with grey scale phase-contrast microscopy showing all cells. (A) to (D) presents cells with wild-type connexin 31 protein, and cells in (E) to (H) contain the mutant protein linked to deafness/neuropathy. The red Alexa Fluor dye was microinjected into the cells marked with ∗ (A, B, E, and F initially), and the dye spreads to adjacent green cells with the wild-type protein, whereas in the case of the mutant protein, the spread is significantly limited (C, D, G, H 33 min later).

4.2. Fluorescence Correlation Spectroscopy

The theory of Fluorescence Correlation Spectroscopy (FCS) was defined by Madge et al. (Magde et al., 1972) and is a technique that measures fluctuations in fluorescence over time to obtain information on dynamic molecular events over a microsecond-second time scale. A brief introduction to the technique is presented; more detailed descriptions of the theory and applications can be found elsewhere (Hess et al., 2002; Thompson et al., 2002; Visser and Hink, 1999). FCS was used to characterize an empirically developed gene delivery system consisting of DNA, protein, and lipid (Mustapa et al., 2007).

4.2.1. Publication XV: Biophysical characterization of an integrin-targeted lipopolyplex gene delivery vector

Mustapa, M. F., Bell, P. C., Hurley, C. A., Nicol, A., Guenin, E., Sarkar, S., Writer, M. J., Barker, S. E., Wong, J. B., Pilkington-Miksa, M. A., Papahadjopoulos-Sternberg, B., Shamlou, P. A., Hailes, H. C., Hart, S. L., Zicha, D. and Tabor, A. B. (2007). *Biochemistry* **46**, 12930–12944.

Open access link to full text:
https://pubs.acs.org/doi/10.1021/bi701014y

Abstract

Nonviral gene delivery vectors now show good therapeutic potential: however, detailed characterization of the composition and macromolecular organization of such particles remains a challenge. This paper describes experiments to elucidate the structure of a ternary, targeted, lipopolyplex synthetic vector, the LID complex. This consists of a lipid component, Lipofectin (L) (1:1 DOTMA:DOPE), plasmid DNA (D), and a dual-function, cationic peptide component (I) containing DNA condensation and integrin-targeting sequences. Fluorophore-labeled lipid, peptide, and DNA components were used to formulate the vector, and the stoichiometry of the particles was established by fluorescence correlation spectroscopy (FCS). The size of the complex was measured by FCS, and the sizes of LID, L, LD, and ID complexes were measured by dynamic light scattering (DLS). Fluorescence quenching experiments and freeze fracture electron microscopy were then used to demonstrate the arrangement of the lipid, peptide, and DNA components within the complex. These experiments showed that the cationic portion of the peptide, I, interacts with the plasmid DNA, resulting in a tightly condensed DNA-peptide inner core; this is surrounded by a disordered lipid layer, from which the integrin-targeting sequence of the peptide partially protrudes.

Author comments on publication XV (Mustapa et al., 2007)

In this corresponding author publication, the author contributed by FCS to the characterization of a gene delivery vector. The contribution involved measurements with Confocor (Zeiss), featuring photon counting abilities, which are essential for the FCS determination of the fluorescence intensity, and the development of evaluation algorithms, including bespoke software presented in Appendix C.

FCS is a technique evaluating fluorescence fluctuations in order to reveal diffusion coefficients, molecular interactions, and concentrations. The time correlations of thermodynamic concentration fluctuations produced by FCS can be interpreted to give kinetic data on chemical reactions, binding constants for various host-guest interactions, information on the diffusion behavior of molecules or particles, and hydrodynamic particle radii. In order to analyze the time course of

fluctuations of the fluorescence intensity $I(t)$ with respect to the time-average fluorescence $\langle I(t)\rangle$, the autocorrelation function is given by Equation

$$G(\tau) = \frac{\langle \delta I(t)\delta I(t+\tau)\rangle}{\langle I(t)\rangle^2} = \frac{\langle I(t)I(t+\tau)\rangle}{\langle I(t)\rangle^2} - 1 \tag{45}$$

where $\delta I(t) = I(t) - \langle I(t)\rangle$ is the deviation from the mean intensity and τ is the autocorrelation time lag. These fluctuations are either derived from changes in the number of fluorescent particles in the confocal volume or changes in the fluorescence yield of the particles. In our experiments, the fluorophores were excited with a laser possessing a Gaussian beam profile, and therefore the confocal volume can be approximated by a Gaussian distribution in the three Cartesian coordinate axes. The true probe volume is further defined as a Gaussian laser beam profile and a pinhole that spatially filters the emitted fluorescence. From this, it is possible to derive a term describing the confocal volume, a structure parameter *SP*, according to Equation

$$SP = \frac{\omega_2}{\omega_1} \tag{46}$$

where ω_2 corresponds to the length of the confocal volume and ω_1 is its width.

In theory, this should remain constant; however, variations in the calibration of the machine lead to small variations in the size of the focus and the pinhole and variations in *SP*. A single particulate species leads to the autocorrelation function to be described by Equation

$$G(\tau) = 1 + \frac{\frac{1}{\sqrt{1+\frac{\tau}{SP^2\tau_{\text{diff}}}}}\left(F_{\text{trip}}e^{-\frac{\tau}{\tau_{\text{trip}}}} + (1-F_{\text{trip}})\right)}{N\left(1-F_{\text{trip}}\right)\left(1+\frac{\tau}{\tau_{\text{diff}}}\right)} \tag{47}$$

where τ_{diff} is the diffusion time, N is the mean number of fluorescent particles diffusing through the detection volume, F_{trip} is the fraction of particles that have entered the triplet state, and τ_{trip} is the corresponding triplet state relaxation time. For a two-component system, however, the definition is given by Equation

$$G(\tau) = 1 + \frac{1}{N\left(1-F_{\text{trip}}\right)}F_{\text{comp}}g_{3\text{di}}(\tau_1) + (1-F_{\text{comp}})g_{3\text{di}}(\tau_2)(F_{\text{trip}}e^{-\frac{\tau}{\tau_{\text{trip}}}} + 1 - F_{\text{trip}}) \tag{48}$$

where

$$g_{3\text{di}}(\tau) = \left(1+\frac{\tau}{\tau_{\text{diff}}}\right)^{-1}\left(1+\frac{\tau}{SP^2\tau_{\text{diff}}}\right)^{-\frac{1}{2}} \tag{49}$$

and F_{comp} is the fraction of the first component, and τ_1 and τ_2 are the diffusion times of the first and second component, respectively.

The measured FCS fluctuation data from the vector were processed using FCS+plus (Evotec Biosystems GmbH) in order to produce the autocorrelation function from each observation.

The obtained autocorrelation functions were fitted to a two-component symbolic function in Mathematica, and the mean values of τ_{diff} was then calculated.

The hydrodynamic radii of the particles can be determined from the measured diffusion times, in order to be compared to the observed light scattering data and information obtained by other microscopy techniques.

Using free Texas Red dye, the author derived ω_1 (the width of the confocal volume) from Equation 50 as its diffusion coefficient is known (2.56238×10^{-10} m^2 s^{-1}).

$$\omega_1 = \sqrt{4D\tau_{\text{diff}}} \tag{50}$$

The diffusion coefficient of the particle was determined after rearranging Equation 50 to yield Equation 51.

$$D = \frac{\omega_1^2}{4\tau_{\text{diff}}} \tag{51}$$

Utilizing the Stokes-Einstein Equation 52, where k is the Boltzman constant, T is temperature, and η is the viscosity, the author derived the radius of the particles as 38.5 nm, which was in good agreement with measurements based on the other techniques presented in the publication. The SI units of the variables are checked in the Appendix C.

$$r = \frac{kT}{6\pi\eta D} \tag{52}$$

4.3. Fluorescence Resonance Energy Transfer

Colocalization of two fluorescently labeled molecular species does not necessarily imply their interactions since standard fluorescence microscopy is not able to resolve their distances in molecular complexes due to Abbe's diffraction limit. Fluorescence Resonance Energy Transfer (FRET) is a technique overcoming the limitation (Bastiaens and Squire, 1999; Sekar and Periasamy, 2003) as it is based on electromagnetic induction, which is a non-radiant process. When two fluorescent dyes are in close proximity, ~10 nm, typical for interacting molecules, the energy is transferred from the higher energy excited fluorochrome to the other dye. Detection of this phenomenon provided information about the molecular interactions and was used to characterize the mutant disease-determining connexins 31 (Di et al., 2005).

4.3.1. Publication XVI: Connexin interaction patterns in keratinocytes revealed morphologically and by FRET analysis

Di, W. L., Gu, Y., Common, J. E., Aasen, T., O'Toole, E. A., Kelsell, D. P. and Zicha, D. (2005). *J Cell Sci* **118**, 1505–1514.

Open access link to full text:
https://journals.biologists.com/jcs/article/118/7/1505/28759

Abstract
Multiple connexins, the major proteins of gap junctions, have overlapping expression in the human epidermis and are postulated to have a key role in keratinocyte differentiation and homeostasis. The functional importance of connexins in the epidermis is emphasised by the association of mutations in four human connexins with various hyperproliferative skin disorders. As immunohistochemistry demonstrated overlapping expression of specific connexins in keratinocytes, we performed colocalisation analyses and applied a modified FRET methodology to assess possible heteromeric interactions between different combinations of four wild-type (wt) and

mutant connexins. The data generated indicate that there is evidence for multiple connexin interactions at the plasma membrane between (wt)Cx26, (wt)Cx30 and (wt)Cx31 in keratinocytes and thus, the potential for the formation of a large number of different channel types each with different channel properties. In addition, we demonstrate that the inherent in vitro trafficking defect of the skin disease mutations (D50N)Cx26 and (G11R)Cx30 can be overcome partially by the coexpression of different wild-type connexins but this rescue does not result in large gap junction aggregates at the plasma membrane. These data indicate that skin disease associated Cx26 or Cx30 mutations are likely to disrupt a number of different channel types important in distinct aspects of keratinocyte biology.

Author comments on publication XVI (Di et al., 2005)

In this corresponding author publication, the author used his previously developed FRET analysis (Gu et al., 2004) and revealed patterns of interactions between mutant connexins in keratinocytes.

4.3.2. Publication XVII: Quantitative fluorescence resonance energy transfer (FRET) measurement with acceptor photobleaching and spectral unmixing

Gu, Y., Di, W. L., Kelsell, D. P. and Zicha, D. (2004). *J. Microsc.* **215**, 162–173.

Open access link to full text:

https://onlinelibrary.wiley.com/doi/full/10.1111/j.0022-2720.2004.01365.x

Abstract

Fluorescence resonance energy transfer (FRET) by acceptor photobleaching is a simple but effective tool for measurements of protein–protein interactions. Until recently, it has been restricted to qualitative or relative assessments owing to the spectral bleed-through contamination resulting from fluorescence overlap between the donor and the acceptor. In this paper, we report a quantitative algorithm that combines the spectral unmixing technique with FRET by acceptor photo-bleaching. By spectrally unmixing the emissions before and after photobleaching, it is possible to resolve the spectral bleed-through and retrieve the FRET efficiency/interaction distance quantitatively. Using a human keratinocyte cell line transfected with cyan fluorescent protein (CFP)- and yellow fluorescent protein (YFP)-tagged Cx26 connexins as an example, FRET information at homotypic gap junctions is measured and compared with well-established methods. Results indicate that the new approach is sensitive, flexible, instrument independent and solely FRET dependent. It can achieve FRET estimations similar to that from a sensitized emission FRET method. This approach has a great advantage in providing the relative concentrations of the donor and the acceptor; this is, for example, very important in the comparative study of cell populations with variable expression levels.

Author comments on publication XVII (Gu et al., 2004)

Connexin proteins fused to either Cyan Fluorescent Protein (CFP) or Yellow Fluorescent Protein (YFP) were introduced into keratinocytes in tissue culture. The introduced connexins interact with each other and form channels at the cell-cell contacts. Fixed keratinocytes with labeled connexins were imaged using laser scanning confocal microscope LSM 510 META (Zeiss) with 458 nm line of the Argon laser and eight spectral channels (emission central wavelengths: 480, 491, 501, 512, 523, 534, 544 and 555 nm). Fifteen spectral stacks were taken before selected Regions Of Interest (ROIs) were photo-bleached with the 514 nm laser line from the Argon laser, and additional 15 images were taken after the bleaching. With closed interaction between CFP and YFP labeled connexins, the FRET causes a reduction in the donor (CFP) fluorescence as its energy is

transferred to the adjacent acceptor (YPF) molecule by a non-radiant process. When the acceptor is selectively photo-damaged, the donor is released from FRET, and its intensity increases, as demonstrated in Figure 20. This increase is unequivocal proof of FRET and close interaction between the molecules at a range below 10 nm. The intensity changes can be used to measure the FRET efficiency, which reflects the ability of the proteins to interact in covalent bonds. The approach is referred to as acceptor depletion FRET (adFRET).

One problem in the measurements is the bleed-through of the signals into the wrong channels. This was eliminated by linear unmixing, which can be expressed as Equation

$$F_{\mathrm{m}}(x,y,\lambda) = d(x,y)F_{\mathrm{d}}(\lambda) + a(x,y)F_{\mathrm{a}}(\lambda) \tag{53}$$

where $d(x, y)$ and $a(x, y)$ are unknown abundance factors of the two fluorochromes at pixel location (x, y), whose spectral responses are expressed as $F_{\mathrm{d}}(\lambda)$ and $F_{\mathrm{a}}(\lambda)$, respectively (subscripts d and a imply the donor and the acceptor), and $F_{\mathrm{m}}(x, y, \lambda)$ is the spectral response of a test sample, which is normalized for the detected emission to eliminate the variation influence of absolute intensities. $F_{\mathrm{d}}(\lambda)$ and $F_{\mathrm{a}}(\lambda)$ are measured using single fluorochrome specimens (controls). Estimations of $d(x, y)$ and $a(x, y)$ were evaluated by the least-squares technique introducing unmixing adFRET (u-adFRET).

FRET efficiency, E, is calculated from Equation

$$E = \frac{d^{\mathrm{ph}}(x,y) - d(x,y)}{d^{ph}(x,y)} \tag{54}$$

where $d^{\mathrm{ph}}(x,y)$ is the donor abundance after photo-bleaching.

All processing was implemented in Mathematica.

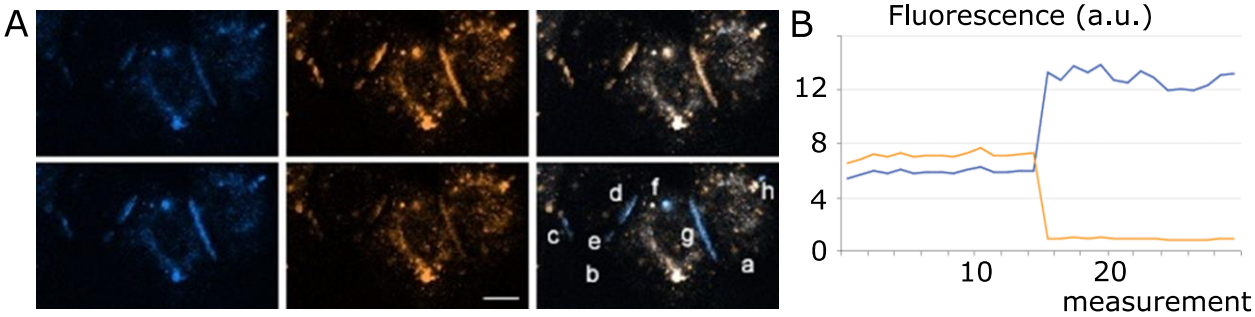

Figure 20. u-adFRET assay using keratinocytes with introduced proteins.(A) (wt)Cx30-CFP (cyan pseudocolour, donor) and (wt)Cx26-YFP (yellow pseudocolour, acceptor). Expression patterns of (wt)Cx30-CFP (left), (wt)Cx26-YFP (middle), and the merged image (right) before bleaching (top row) and the changes of fluorescence intensity in areas of interest (c to h) after bleaching (bottom row) show enhanced fluorescence intensity of donor (cyan pseudocolor, left) and reduced fluorescence intensity of acceptor (yellow pseudocolor, middle). Cyan and yellow pseudocolor look-up tables were designed to produce white in the merged image when perfectly colocalized. Areas labeled a and b were used as a background reference and an unbleached reference, respectively. Scale bar 10 µm. (B) Example changes of fluorescence intensity in the donor (cyan) and acceptor (yellow) before (the first 15 measurements) and after photo-bleaching (the second 15 measurements).

Continuation of author comments on publication XVI (Di et al., 2005)

In the Journal of Cell Science publication XVI, the u-adFRET assay was applied to a range of different pairs of connexin proteins, and their ability to interact was quantified (Table 3). The fairly high efficiency of binding between the mutant (G11R, D50N) and the wild-type connexins 31 indicates their ability to disrupt the intercellular gap junction channels they form.

Connexin combination	Number of cells	Number of ROIs	FRET efficiency mean ± SD [%]
(wt)Cx30+(wt)Cx30	33	59	37 ± 13
(wt)Cx31+(wt)Cx31	26	51	36 ± 11
(wt)Cx26+(wt)Cx30	51	102	32 ± 15
(wt)Cx26+(wt)Cx26	35	66	24 ± 13
(wt)Cx30+(wt)Cx31	63	94	23 ± 15
(wt)Cx31+(wt)Cx30.3	37	92	21 ± 14
(wt)Cx26+(wt)Cx30.3	38	108	19 ± 15
(wt)Cx26+(wt)Cx31	65	117	15 ± 11
(wt)Cx30+(wt)Cx30.3	26	74	14 ± 10
(wt)Cx30.3+(wt)Cx30.3	16	47	9 ± 7
(wt)Cx30+(G11R)Cx30	42	142	29 ± 13
(wt)Cx26+(G11R)Cx30	44	187	26 ± 14
(wt)Cx26+(D50N)Cx26	27	135	24 ± 12
(wt)Cx31+(G11R)Cx30	37	137	22 ± 12
(wt)Cx31+(D50N)Cx26	44	260	21 ± 14
(wt)Cx30+(D50N)Cx26	28	129	20 ± 13

Table 3. FRET efficiencies calculated for connexin combinations. (wt) stands for wild-type, and G11R and D50N are single-point mutations. SD stands for Standard Deviation.

4.4. Fluorescence Localization After Photobleaching

A newly developed technique of Fluorescence Localization After Photobleaching (FLAP) led to the discovery of active transport of monomeric actin into protrusions of metastatic cancer cells (Zicha et al., 2003). This transport was missing in previous models of cell motility (Pollard and Borisy, 2003; Pollard and Cooper, 2009).

4.4.1. Publication XVIII: Rapid actin transport during cell protrusion

Zicha, D., Dobbie, I. M., Holt, M. R., Monypenny, J., Soong, D. Y. H., Gray, C. and Dunn, G. A. (2003). *Science* **300**, 142–145.

Open access link to full text:
https://www.science.org/doi/10.1126/science.1082026

Abstract

Transformed rat fibroblasts expressing two variants of green fluorescent protein, each fused to actin, were used to study actin dynamics during cell protrusion. The recently developed FLAP(fluorescence localization after photobleaching) method permits the tracking of one fluorophore after localized photobleaching by using the other as a colocalized reference. Here, by visualizing the ratio of bleached to total molecules, we found that actin was delivered to protruding zones of the leading edge of the cell at speeds that exceeded 5 micrometers per second. Monte Carlo modeling confirmed that this flow cannot be explained by diffusion and may involve active transport.

Author comments on publication XVIII (Zicha et al., 2003)

This first-author publication has acquired 131 citations to date. The FLAP technique is based on imaging double-labeled molecular species in two channels, photobleaching one of the labels in a defined Region Of Interest (ROI), and quantitatively evaluating the dynamics. The technique reveals information about dynamic localization: where the molecules are being delivered to, inside live cells, including relative concentrations. The publication reports on the use of CFP-actin and YFP-actin introduced into the metastatic T15 cells. Images were acquired using LSM 510 (Zeiss) in multitracking mode. The two fluorescence channels were thus acquired with a minimal delay at 1 ms lag. Pixel intensity in the YFP channel reflects the number of fluorescent actin molecules according to Equation

$$\frac{I_{\mathrm{YFP}}}{\sum I_{\mathrm{YFP}}} = \frac{n_{\mathrm{YFP}}}{N_{\mathrm{YFP}}} \tag{55}$$

where I is pixel intensity, ΣI is integrated cell intensity, n is the number of molecules in the pixel, and N is the number of molecules in the cell. The YFP was selectively bleached with high intensity of the 514 nm line from the argon laser in a defined ROI, as illustrated in Figure 21 and reflected in Equation

$$\frac{I_{\mathrm{YFP}}}{\sum I_{\mathrm{YFP}}} = \frac{n_{\mathrm{YFP}} - n^*_{\mathrm{YFP}}}{N_{\mathrm{YFP}}} \tag{56}$$

where n^* is the number of bleached molecules. Since the YFP molecules localize with the CFP molecules and their intensities are matched, ΣI_{YFP} can be substituted with ΣI_{CFP} (Equation 57).

$$\frac{I_{\mathrm{YFP}}}{\sum I_{\mathrm{CFP}}} = \frac{n_{\mathrm{YFP}} - n^*_{\mathrm{YFP}}}{N_{\mathrm{YFP}}} \tag{57}$$

Substitution of I_{YFP} requires the introduction of an expected number of molecules $\langle n \rangle$ since the incidence within a pixel is a stochastic process (Equation 58).

$$\frac{I_{\mathrm{CFP}}}{\sum I_{\mathrm{CFP}}} = \frac{\langle n_{\mathrm{YFP}} \rangle}{N_{\mathrm{YFP}}} \tag{58}$$

Subtraction of Equation 57 from Equation 58 reveals that the calculated Absolute FLAP (a-FLAP) and provides the expected information about the number of bleached molecules at a given pixel and acquisition time (Equation 59).

$$\frac{I_{\mathrm{CFP}} - I_{\mathrm{YFP}}}{\sum I_{\mathrm{CFP}}} = \frac{\langle n^*_{\mathrm{YFP}} \rangle}{N_{\mathrm{YFP}}} \tag{59}$$

The most interesting results came after the introduction of Relative FLAP (r-FLAP) derived by ratioing of Equation 59 and Equation 58 presented in Equation 60.

$$\frac{I_{\mathrm{CFP}} - I_{\mathrm{YFP}}}{I_{\mathrm{CFP}}} = \frac{\langle n^*_{\mathrm{YFP}} \rangle}{\langle n_{\mathrm{YFP}} \rangle} \tag{60}$$

The difference between the CFP image and YFP image ratioed by the CFP image provides information about the expected relative number of bleached molecules at the location at the

acquisition time.

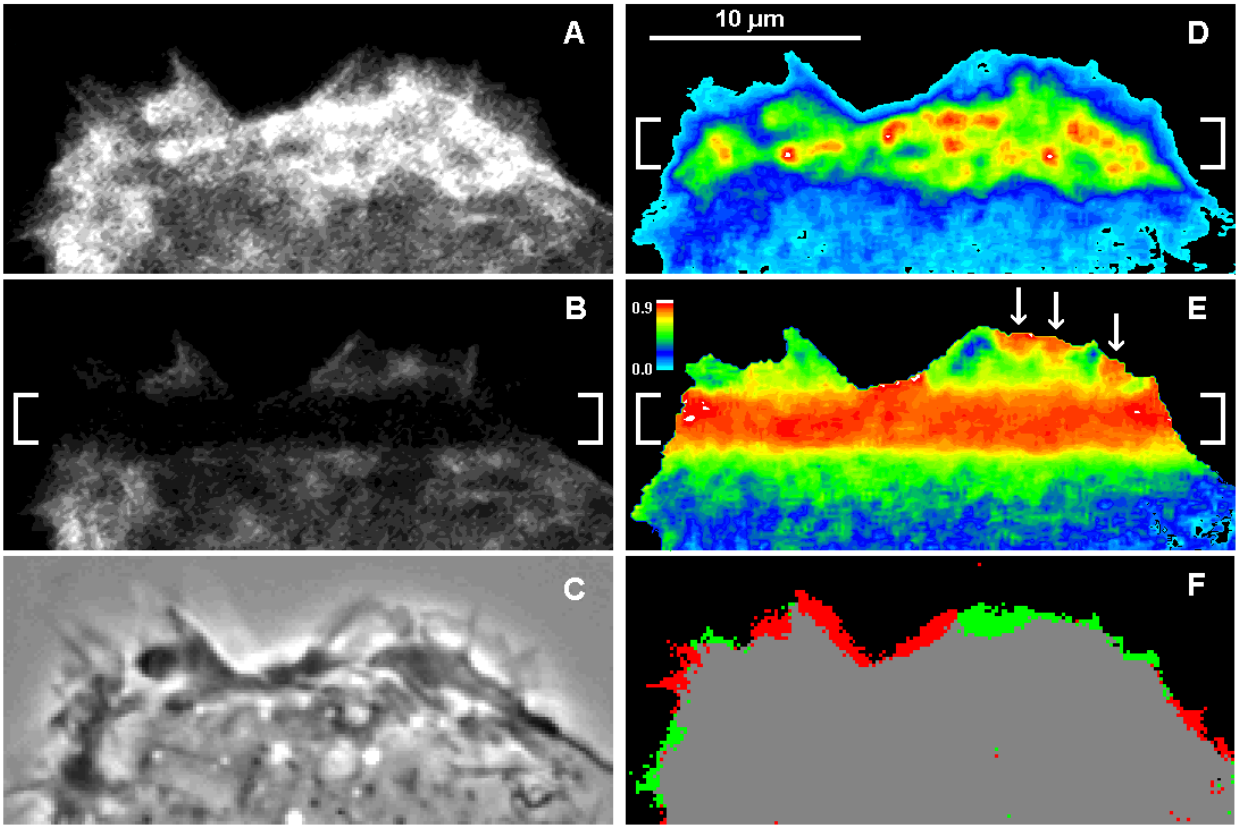

Figure 21. FLAP illustration. (A) is an image of CPF distribution in the leading part of the metastatic cell T15. (B) is an image of YFP distribution in the first frame after photobleaching between the white brackets. (C) is a phase-contrast image of the same part of the cell. (D) shows a-FLAP image calculated by subtracting B from A. (E) presents r-FLAP calculated by ratioing D, and A. White arrows indicate areas of rapid actin delivery in the protrusion areas. (F) shows protrusions (newly allocated area) in green and retractions (areas occupied previously which are no more occupied) in red. Pseudocolor mapping of FLAP signal is represented in the bar (E)

Figure 21 shows that a-FLAP signal distribution (D) is very similar to the CFP distribution (A), which is not surprising since the bleached YPF-actin molecules are expected at places with a high incidence of all the actin molecules identified by CFP-actin molecules. Only the r-FLAP reveals a very high proportion of bleached molecules rapidly transported into the protrusion areas (white arrows in E) with limited material dominated by the CFP-actin molecules. Monte-Carlo simulation showed that this rapid transport cannot be explained by diffusion and trapping of molecules in the periphery and proved that active transport of actin molecules must be present in these rapidly moving metastatic cells.

5. CONCLUSIONS

This habilitation thesis presents an overview of the scientific research of the author with comments on the relevant principles and their applications. The projects are grouped into two sections focusing on similar concepts with 18 authored and co-authored publication references.

The first section on cell motility and invasion presents changes in motility, chemotaxis, and invasion of metastatic cells identifying a novel metastasis suppressor, protein 4.1B, and contributing to revealing the function of GAB1 function in motility and morphology of leukemia cells. This used the theory of moments, diffusion theory, interference theory, and statistics of directional data. The role of kindlin-3 protein in the efficient migration of B-cells was identified using a novel tracking algorithm. The importance of ephrin-B2 protein as a motility and morphology modulator was shown in endothelial cells by measuring their speed and morphology. Graph theory was used to develop a novel indirect cell motility assay based on the minimal spanning tree.

The second area of concepts, focused on intracellular motion and characterization of molecules, presents the identification of molecular mechanisms for deafness/neuropathy and skin disease related to mutations of connexin 31, by showing defects of cell-cell transport of small molecules and induced cell death using bespoke quantitation of dynamic fluorescence imaging. The ability of the mutant connexins 31 to interact and form molecular complexes important for their physiological function was mapped using a specifically developed unmixing acceptor depletion FRET algorithm. Fluorescence correlation spectroscopy was used to characterize a transfection vector, and its molecular size was measured. Rapid intracellular transport of actin monomer in metastatic cells was revealed by a newly developed technique of FLAP based on two-channel imaging and selective photo-bleaching. The processing was based on the algebra of random variables.

The future projects will mainly focus on developments of Holographic Incoherent-light-source Quantitative Phase Imaging (hiQPI) and its applications, especially in cancer research. Correlative microscopy will be another important field combining hiQPI and other imaging modalities, such as laser scanning confocal microscopy. The developments will include novel observation chambers and 3D imaging. Significant progress is expected with the development and implementation of image processing and data analysis algorithms specific for the hiQPI and correlative microscopy. BSc, MSc and Ph.D. students will be recruited to get involved in the projects mentioned above. The experience gained in this research and development will enrich teaching microscopy, spectroscopy and biophotonics, and strengthen interdisciplinary topics within the study programmes of Physical Engineering and Nanotechnology (B-FIN-P, N-FIN-P, D-FIN-P) and Precise Mechanics and Optics (N-PMO-P) at the Faculty of Mechanical Engineering, Brno University of Technology.

6. REFERENCES

Abrams, C. K., Freidin, M. M., Verselis, V. K., Bargiello, T. A., Kelsell, D. P., Richard, G., Bennett, M. V. L. and Bukauskas, F. F. (2006). Properties of Human Connexin 31, Which Is Implicated in Hereditary Dermatological Disease and Deafness. *Proc. Natl. Acad. Sci. U. S. A.* **103**, 5213–5218.

Alt, W. (Wolfgang) (1990). *Biological motion : proceedings of a workshop held in Königswinter, Germany, March 16-19, 1989 / W. Alt, G. Hoffmann (editor).* 1st ed. 19. Berlin : Berlin .

Bastiaens, P. I. and Squire, A. (1999). Fluorescence lifetime imaging microscopy: spatial resolution of biochemical processes in the cell. *Trends Cell Biol.* **9**, 48–52.

Carpenter, A. E., Jones, T. R., Lamprecht, M. R., Clarke, C., Kang, I. H., Friman, O., Guertin, D. A., Chang, J. H., Lindquist, R. A., Moffat, J., Golland, P. and Sabatini, D. M. (2006). CellProfiler: image analysis software for identifying and quantifying cell phenotypes. *Genome Biol.* **7**, R100.

Cavanna, T., Pokorná, E., Veselý, P., Gray, C. and Zicha, D. (2007). Evidence for protein 4.1B acting as a metastasis suppressor. *J. Cell Sci.* **120**, 606–616.

Crank, J. (1975). *The mathematics of diffusion*. 2nd ed. Clarendon Press Oxford [England].

Creath, K. (1988). V Phase-Measurement Interferometry Techniques. In (ed. Wolf, E. B. T.-P. in O.), pp. 349–393. Elsevier.

Dalecká, M., Sabó, J., Backová, L., Rösel, D., Brábek, J., Benda, A. and Tolde, O. (2021). Invadopodia Structure in 3D Environment Resolved by Near-Infrared Branding Protocol Combining Correlative Confocal and FIB-SEM Microscopy. *Int. J. Mol. Sci.* **22**,.

Davies, H. G. and Wilkins, M. H. (1952). Interference microscopy and mass determination. *Nature* **169**, 541.

Di, W. L., Monypenny, J., Common, J. E., Kennedy, C. T., Holland, K. A., Leigh, I. M., Rugg, E. L., Zicha, D. and Kelsell, D. P. (2002). Defective trafficking and cell death is characteristic of skin disease-associated connexin 31 mutations. *Hum Mol Genet* **11**, 2005–2014.

Di, W. L., Gu, Y., Common, J. E., Aasen, T., O'Toole, E. A., Kelsell, D. P. and Zicha, D. (2005). Connexin interaction patterns in keratinocytes revealed morphologically and by FRET analysis. *J Cell Sci* **118**, 1505–1514.

Dunn, G. A. and Zicha, D. (1993). Phase-Shifting Interference Microscopy Applied to the Analysis of Cell Behavior. *Cell Behav. Adhes. Motil.* **47**, 91–106.

Edelstein, A., Amodaj, N., Hoover, K., Vale, R. and Stuurman, N. (2010). Computer control of microscopes using microManager. *Curr Protoc Mol Biol* **Chapter 14**, Unit14 20.

Fares, J., Fares, M. Y., Khachfe, H. H., Salhab, H. A. and Fares, Y. (2020). Molecular principles of metastasis: a hallmark of cancer revisited. *Signal Transduct. Target. Ther.* **5**, 28.

Foo, S. S., Turner, C. J., Adams, S., Compagni, A., Aubyn, D., Kogata, N., Lindblom, P., Shani, M., Zicha, D. and Adams, R. H. (2006). Ephrin-B2 controls cell motility and adhesion during blood-vessel-wall assembly. *Cell* **124**, 161–173.

Gu, Y., Di, W. L., Kelsell, D. P. and Zicha, D. (2004). Quantitative fluorescence resonance energy transfer (FRET) measurement with acceptor photobleaching and spectral unmixing. *J.*

Microsc. **215**, 162–173.

Hagglund, S., Hoppe, A., Aubyn, D., Cavanna, T., Jordan, P. and Zicha, D. (2009). Novel shear flow assay provides evidence for non-linear modulation of cancer invasion. *Front Biosci (Landmark Ed)* **14**, 3085–3093.

Hess, S. T., Huang, S., Heikal, A. A. and Webb, W. W. (2002). Biological and chemical applications of fluorescence correlation spectroscopy: a review. *Biochemistry* **41**, 697–705.

Huang, Y. L., Ma, Y., Wu, C., Shiau, C., Segall, J. E. and Wu, M. (2020). Tumor spheroids under perfusion within a 3D microfluidic platform reveal critical roles of cell-cell adhesion in tumor invasion. *Sci. Rep.* **10**, 9648.

Jin, T., Xu, X. and Hereld, D. (2008). Chemotaxis, chemokine receptors and human disease. *Cytokine* **44**, 1–8.

Jones, G. E., Zicha, D., Dunn, G. A., Blundell, M. and Thrasher, A. (2002). Restoration of podosomes and chemotaxis in Wiskott-Aldrich syndrome macrophages following induced expression of WASp. *Int J Biochem Cell Biol* **34**, 806–815.

Kolman, P. and Chmelik, R. (2010). Coherence-controlled holographic microscope. *Opt Express* **18**, 21990–22003.

Magde, D., Elson, E. and Webb, W. W. (1972). Thermodynamic Fluctuations in a Reacting System---Measurement by Fluorescence Correlation Spectroscopy. *Phys. Rev. Lett.* **29**, 705–708.

Mardia, K. V (1975). Statistics of Directional Data. *J. R. Stat. Soc. Ser. B* **37**, 349–393.

Meyer, A. S., Hughes-Alford, S. K., Kay, J. E., Castillo, A., Wells, A., Gertler, F. B. and Lauffenburger, D. A. (2012). 2D protrusion but not motility predicts growth factor-induced cancer cell migration in 3D collagen. *J. Cell Biol.* **197**, 721–729.

Mustapa, M. F., Bell, P. C., Hurley, C. A., Nicol, A., Guenin, E., Sarkar, S., Writer, M. J., Barker, S. E., Wong, J. B., Pilkington-Miksa, M. A., Papahadjopoulos-Sternberg, B., Shamlou, P. A., Hailes, H. C., Hart, S. L., Zicha, D. and Tabor, A. B. (2007). Biophysical characterization of an integrin-targeted lipopolyplex gene delivery vector. *Biochemistry* **46**, 12930–12944.

Pollard, T. D. and Borisy, G. G. (2003). Cellular motility driven by assembly and disassembly of actin filaments. *Cell* **112**, 453–465.

Pollard, T. D. and Cooper, J. A. (2009). Actin, a central player in cell shape and movement. *Science* **326**, 1208–1212.

Seda, V., Vojackova, E., Ondrisova, L., Kostalova, L., Sharma, S., Loja, T., Pavlasova, G. M., Zicha, D., Peskova, M. K., Krivanek, J., Liskova, K., Kren, L., Benes, V., Litzmanova, K. M., Borsky, M., Oppelt, J., Verner, J., Pospisilova, S., Brychtova, Y., et al. (2021). FoxO1-GAB1 axis regulates homing capacity and tonic AKT activity in chronic lymphocytic leukemia. *Blood* **138**, 758–772.

Sekar, R. B. and Periasamy, A. (2003). Fluorescence resonance energy transfer (FRET) microscopy imaging of live cell protein localizations. *J. Cell Biol.* **160**, 629–633.

Slabý, T., Antoš, M., Dostál, Z., Kolman, P. and Chmelík, R. (2010). Coherence-controlled holographic microscope. In *Proceedings of SPIE - The International Society for Optical Engineering*, p. 77461R.

Tattersall, D., Scott, C. A., Gray, C., Zicha, D. and Kelsell, D. P. (2009). EKV mutant connexin 31 associated cell death is mediated by ER stress. *Hum Mol Genet* **18**, 4734–4745.

Thompson, N. L., Lieto, A. M. and Allen, N. W. (2002). Recent advances in fluorescence correlation spectroscopy. *Curr. Opin. Struct. Biol.* **12**, 634–641.

Visser, A. J. W. G. and Hink, M. A. (1999). New Perspectives of Fluorescence Correlation Spectroscopy. *J. Fluoresc.* **9**, 81–87.

Willenbrock, F., Zicha, D., Hoppe, A. and Hogg, N. (2013). Novel automated tracking analysis of particles subjected to shear flow: Kindlin-3 role in B cells. *Biophys. J.* **105**, 1110–1122.

Zicha, D. (2022). Addressing cancer invasion and cell motility with quantitative light microscopy. *Sci. Rep.* **12**, 1621.

Zicha, D. and Dunn, G. A. (1995). An image-processing system for cell behavior studies in subconfluent cultures. *J. Microsc. Oxford* **179**, 11–21.

Zicha, D. and Pardo, O. E. (2009). High content screening and analysis. *Eur. Pharm. Rev.* **14**, 38–45.

Zicha, D., Dunn, G. A. and Brown, A. F. (1991). A new direct-viewing chemotaxis chamber. *J. Cell Sci.* **99**, 769–775.

Zicha, D., Allen, W. E., Brickell, P. M., Kinnon, C., Dunn, G. A., Jones, G. E. and Thrasher, A. J. (1998). Chemotaxis of macrophages is abolished in the Wiskott-Aldrich syndrome. *Br J Haematol* **101**, 659–665.

Zicha, D., Dobbie, I. M., Holt, M. R., Monypenny, J., Soong, D. Y. H., Gray, C. and Dunn, G. A. (2003). Rapid actin transport during cell protrusion. *Science* **300**, 142–145.

APPENDIX A: Micromanager phase-shifting Bash script

```
 * Script to acquire phase-shifting interference image sequences
 * using wedge stepper motor, RS stepper motor control board 718-846 and
 * Hamamatsu C4742-95-12ERG camera
 * Set Multi-dimensional Acquisition Number of Time points 10,
 * Interval 30 ms, Required Directory root and Name prefix
 * Set up the numbers below and run the script
 * Daniel Zicha
import ij.ImagePlus;
// Number of timepoints e.g. 1322 or 3 or 4
nrFrames = 1441;
// Time between timePoints (in ms e.g. 60000 or 4000);
intervalMs = 60000;
burstExposure = 30.0;
burstChannel = "Horn";
port = "COM1";
//micrometer start: 4 shaft notches visible and 0 on Vernier
initialiseStepper1="P 10000 14960 40000 40000";
initialiseStepper2="R2";
openShutter = "O1";
closeShutter = "O0";
energise = "E8";
startPhaseShifting = "M19000";
rewind = "M-19000";
deenergise = "E0";
delay1 = 100;
delay2 = 100;
delay3 = 2500;
ImagePlus DisplayedImage = new ImagePlus();
mmc.setExposure(burstExposure);
mmc.setConfig("Channel", burstChannel);
mmc.setSerialPortCommand(port, initialiseStepper1, "\r\n");
mmc.setSerialPortCommand(port, initialiseStepper2, "\r\n");
mmc.setSerialPortCommand(port, deenergise, "\r\n");
for (frame=0; frame < nrFrames; frame++) {
        now = System.currentTimeMillis();
        mmc.setSerialPortCommand(port, energise, "\r\n");
```

```
        mmc.setSerialPortCommand(port, openShutter, "\r\n");
        mmc.waitForSystem();
        mmc.setSerialPortCommand(port, startPhaseShifting, "\r\n");
        gui.sleep(delay1);
        mmc.waitForSystem();
        mmc.waitForSystem();
        gui.startBurstAcquisition();
        gui.sleep(delay2);
        mmc.setSerialPortCommand(port, closeShutter, "\r\n");
        mmc.setSerialPortCommand(port, rewind, "\r\n");
        gui.sleep(delay3);
        mmc.setSerialPortCommand(port, deenergise, "\r\n");
        gui.closeAllAcquisitions();
        itTook = System.currentTimeMillis() - now;
        if ((intervalMs - itTook) > 0)
                gui.sleep(intervalMs - itTook);
        DisplayedImage = ij.IJ.getImage();
        img = DisplayedImage.getImage();
        img1=img.getData();
        db=img1.dataBuffer;
        num1=img1.data[0];
        num2=img1.data[1];
        directory=acq.rootName_;
        gui.message(directory);
        FileInputStream fstream = new
        FileInputStream("c://Users//zicha01//AcquisitionData//drift.dat");
        DataInputStream instream = new DataInputStream(fstream);
        BufferedReader br = new BufferedReader(new InputStreamReader(instream));
        Line = br.readLine();
        br.close();
        n1=eval(Line);
        n2=n1+1;
        gui.message(Line);
        gui.message(n2);
        print(n2);
        exec("dir " + directory);
        DisplayedImage.close();
}
```

APPENDIX B: Cell Profiler MATLAB module for Scattering Tree

```
function handles = MeasureObjectScatteringTreeFactor(handles)
drawnow
[CurrentModule, CurrentModuleNum, ModuleName] = CPwhichmodule(handles);
ObjectName = char(handles.Settings.VariableValues{CurrentModuleNum,1});
ColoredNeighborsName = char(handles.Settings.VariableValues{CurrentModuleNum,3});
drawnow
IncomingLabelMatrixImage = CPretrieveimage(handles,['Segmented',
ObjectName],ModuleName,'MustBeGray','DontCheckScale');
drawnow
[sr,sc] = size(IncomingLabelMatrixImage);
NumberOfObjects=max(IncomingLabelMatrixImage(:));
l = NumberOfObjects;
distance(1)=-1;
StructuringElement = strel('square',3);
cellOutlineImage=IncomingLabelMatrixImage-
imerode(IncomingLabelMatrixImage,StructuringElement);
if l>1
%%% Cell Scattering Tree based on Minimum Spanning Tree of distances
%%% between cells measuring cell scattering
%%% collect outline coordinates
lengthOfCellOutline=zeros(NumberOfObjects,1);
lm=logical(cellOutlineImage);
estimateOfOutlineSize=round(sum(lm(:))/NumberOfObjects*2.5);
cellOutlineCoordinateX=zeros(NumberOfObjects,estimateOfOutlineSize);
cellOutlineCoordinateY=zeros(NumberOfObjects,estimateOfOutlineSize);
for y = 1:sr
   for x = 1:sc
      pixelValue=cellOutlineImage(y,x);
      if (pixelValue>0)
         lengthOfCellOutline(pixelValue,1)=lengthOfCellOutline(pixelValue,1)+1;
         outlinePixelNumber=lengthOfCellOutline(pixelValue,1);
         cellOutlineCoordinateX(pixelValue,outlinePixelNumber)=x;
         cellOutlineCoordinateY(pixelValue,outlinePixelNumber)=y;
      end;
   end
end
drawnow
```

```
distanceMatrix=ones(NumberOfObjects)*inf;
cellFromOutlineIndexMatrix=zeros(NumberOfObjects);
cellToOutlineIndexMatrix=zeros(NumberOfObjects);
for cellFrom = 1:(NumberOfObjects-1)
   for cellTo = (cellFrom+1):NumberOfObjects
      for cellFromOutlineIndex = 1:lengthOfCellOutline(cellFrom,1)
         for cellToOutlineIndex = 1:lengthOfCellOutline(cellTo,1)
            currentDistance=sqrt((cellOutlineCoordinateX(cellFrom,cellFromOutlineIndex)-
cellOutlineCoordinateX(cellTo,cellToOutlineIndex))^2+...
               (cellOutlineCoordinateY(cellFrom,cellFromOutlineIndex)-
cellOutlineCoordinateY(cellTo,cellToOutlineIndex))^2);
            if currentDistance<distanceMatrix(cellFrom,cellTo)
               distanceMatrix(cellFrom,cellTo)=currentDistance;
               cellFromOutlineIndexMatrix(cellFrom,cellTo)=cellFromOutlineIndex;
               cellToOutlineIndexMatrix(cellFrom,cellTo)=cellToOutlineIndex;
            end;
         end
      end
   end
end
drawnow
a=distanceMatrix;
for i = 1:l-1
   for j = i+1:l
      a(j,i)=a(i,j);
   end
end
%Prims Algorithm
k=1:l;
listV(k)=0;
listV(1)=1;
e=1;
while (e<l)
   min1=inf;
    for i=1:l
      if listV(i)==1
         for j=1:l
            if listV(j)==0
```

```
                if min1>a(i,j)
                    min1=a(i,j);
                    b=a(i,j);
                    s=i;
                    d=j;
                end
            end
        end
    end
    end
    listV(d)=1;
    distance(e)=b;
    source(e)=s;
    destination(e)=d;
    e=e+1;
end

lineX=zeros(l-1,2);
lineY=zeros(l-1,2);
for i=1:l-1
    cellFrom=min(source(i),destination(i));
    cellTo=max(source(i),destination(i));
    cellFromOutlineIndex=cellFromOutlineIndexMatrix(cellFrom,cellTo);
    cellToOutlineIndex=cellToOutlineIndexMatrix(cellFrom,cellTo);
    lineX(i,1)=cellOutlineCoordinateX(cellFrom,cellFromOutlineIndex);
    lineX(i,2)=cellOutlineCoordinateX(cellTo,cellToOutlineIndex);
    lineY(i,1)=cellOutlineCoordinateY(cellFrom,cellFromOutlineIndex);
    lineY(i,2)=cellOutlineCoordinateY(cellTo,cellToOutlineIndex);
end
end
drawnow
        %%% Saves the Cell Scattering Tree Factor
        if ~isfield(handles.Measurements.Image,'ObjectScatteringTreeFactorFeatures')
            handles.Measurements.Image.ObjectScatteringTreeFactorFeatures = {};
            handles.Measurements.Image.ObjectScatteringTreeFactor = {};
        end
```

```
        column =
find(~cellfun('isempty',strfind(handles.Measurements.Image.ObjectScatteringTreeFactorFeatures,
ObjectName)));
        if isempty(column)
            handles.Measurements.Image.ObjectScatteringTreeFactorFeatures(end+1) =
{ObjectName};
            column = length(handles.Measurements.Image.ObjectScatteringTreeFactorFeatures);
        end

handles.Measurements.Image.ObjectScatteringTreeFactor{handles.Current.SetBeingAnalyzed}(1,
column) = sum(distance);
drawnow
ThisModuleFigureNumber = handles.Current.(['FigureNumberForModule',CurrentModule]);
   ColoredIncomingObjectsImage = CPlabel2rgb(handles,IncomingLabelMatrixImage);
   ColoredCellOutlineImage = CPlabel2rgb(handles,cellOutlineImage);
   CPfigure(handles,'Image',ThisModuleFigureNumber);
   if handles.Current.SetBeingAnalyzed == handles.Current.StartingImageSet
      CPresizefigure(IncomingLabelMatrixImage,'TwoByOne',ThisModuleFigureNumber)
   end
   subplot(2,1,1);
   CPimagesc(ColoredIncomingObjectsImage,handles);
   title(ObjectName)
   subplot(2,1,2);
   CPimagesc(ColoredCellOutlineImage,handles);
   title(['Scattering Tree Factor of ', ObjectName, ' = ', num2str(sum(distance))])
   for i=1:l-1
      line(lineX(i,:), lineY(i,:), 'Color', [1 1 1]);
   end
drawnow
```

APPENDIX C: Mathematica code for Fluorescence Correlation Spectroscopy

Single component analysis

```
acfFun[timeLag_, numberOfParticles_, spK_, fTrip_, tauTrip_, tauD_] :=
 1 + 1 / (numberOfParticles * (1 - fTrip)) *
   (1 + timeLag / tauD) ^ -1 * (1 + timeLag / (spK^2 * tauD)) ^ (-1 / 2) *
   (fTrip * Exp[-timeLag / tauTrip] + (1 - fTrip))

NonlinearRegress[Take[corData, {begin, end}],
 acfFun[timeLag, numberOfParticles, spK, fTrip, tauTrip, tauD],
 {timeLag}, {{numberOfParticles, 0.5, 0., 1000.}, {fTrip, 0.1, 0., 1.},
  {tauTrip, 0.004, 0., 1.}, {spK, 5.0, 0., 100.}, {tauD, 0.055, 0., 1.}},
 RegressionReport → {ANOVATable, BestFit, BestFitParameters, EstimatedVariance,
   FitResiduals, ParameterCITable, ParameterTable}, MaxIterations → 100]
```

Two component analysis

```
Clear[g3di];
g3di[timeLag_, spK_, tauD_] :=
 (1 + timeLag / tauD) ^ -1 * (1 + timeLag / (spK^2 * tauD)) ^ (-1 / 2)

Clear[acfFun2];
acfFun2[timeLag_, numberOfParticles_, spK_, fTrip_, tauTrip_,
  tauD1_, tauD2_, comp1_] := 1 + 1 / (numberOfParticles * (1 - fTrip)) *
   (comp1 * g3di[timeLag, spK, tauD1] + (1 - comp1) * g3di[timeLag, spK, tauD2]) *
   (fTrip * Exp[-timeLag / tauTrip] + (1 - fTrip))

NonlinearRegress[Take[corData, {begin, end}],
 acfFun2[timeLag, numberOfParticles, structureParameter,
  fTrip, tauTrip, tauDPeptide, tauD2, comp1], {timeLag},
 {{numberOfParticles, 1.0, 0., 1000.}, {fTrip, 0.1, 0., 1.},
  {tauTrip, 0.003, 0., 1.}, {tauD2, 3.0, 0., 10.},
  {comp1, 0.1, 0., 1.}}, MaxIterations → 100,
 RegressionReport → {ANOVATable, BestFit, BestFitParameters,
   EstimatedVariance, FitResiduals, ParameterCITable,
   ParameterTable}]
```

Radius determination

```
omega1 = √(4 * diffusionCoefficientTexasRed * tauDTexasRed) (*m*)
```

2.6946×10^{-7}

```
omega2 = structureParameter * omega1
```

1.82167×10^{-6}

```
diffusionCoefficientComplex = omega1^2 / (4 * tauDiffComplex) (*m^2/second*)
```

6.37151×10^{-12}

```
k = 1.38 * 10^-23 (*k is the Boltzman constant (1.38*10^-23 JK^-1) *)
```

1.38×10^{-23}

```
t = 298 (*K*)
```

298

```
η = 8.9 * 10^-4 (*where η is the viscosity of the solvent. Use a
    value of 8.9*10^-4 kgm^-1 s^-1 for water at 25 degrees Centigrade*)
```

0.00089

$$\text{rm} = \frac{\text{k} * \text{t}}{6\,\pi\,\eta\,\text{diffusionCoefficientComplex}}$$

3.84735×10^{-8}

Check units

```
Kilo Gram Meter^2 Second^-2 Kelvin^-1
 Kelvin / (Kilo Gram Meter^-1 Second^-1 Meter^2 Second^-1)
```

Meter